Local Inhibitory Dynamics Underpin Temporal Integration and Functional Segregation between Barrels and Septa in the Mouse Barrel Cortex

Ali Özgür Argunşah[1,2], Tevye Jason Stachniak[1,2,3], Jenq-Wei Yang[1,2], Linbi Cai[1,2], Alexander van der Bourg[1,2], Rahel Kastli[1,2,4], Theofanis Karayannis[1,2,5,*]

[1]Laboratory of Neural Circuit Assembly, Brain Research Institute, University of Zurich Winterthurerstrasse 190, CH-8057 Zurich, Switzerland.

[2]Neuroscience Center Zurich, University of Zurich and ETH Zurich, Winterthurerstrasse 190, CH-8057 Zurich, Switzerland.

[3]Division of Biomedical Sciences, Faculty of Medicine, Memorial University of Newfoundland, St. John's, A1B 3V6, Canada.

[4]Department of Stem Cell & Regenerative Biology, Harvard University, Cambridge, MA, USA.

[5]University Research Priority Program (URPP), Adaptive Brain Circuits in Development and Learning, University of Zurich, Zurich, Switzerland.

[*]Correspondence: karayannis@hifo.uzh.ch

Abstract

Just as separated digits and repeated sampling enhance somatosensation in humans, mice sense objects through multiple segregated whiskers through successive contacts. Individual whisker identity is maintained through the somatotopic organization of the Whisker→Brainstem→Thalamus→Cortex axis, culminating in distinct cortical domains: barrels and the surrounding septa. By performing simultaneous recordings using in-vivo electrophysiology in wild-type (WT) mice, we identify a progressive divergence in spiking activity between these domains upon repeated behaviorally relevant (10Hz) single- and multi-whisker stimulation. While the spiking activity ratio of multi- to single-whisker stimulation remains stable in barrels, it increases progressively in septa, suggesting inhibitory cell recruitment. Using genetic fate-mapping and tissue clearing, we indeed reveal that SST+ and VIP+ interneurons exhibit distinct laminar and regional distributions in barrel and septa domains. Further, calcium imaging of SST+ and VIP+ interneurons

shows that while both neuron types respond to single-whisker stimulus, SST+ interneurons preferentially engage more in 10Hz multi-whisker stimulation, indicating their critical role in progressive stimulus preference. Genetic removal of Elfn1, which regulates the incoming excitatory synaptic dynamics onto SST+ interneurons, leads to the loss of the progressive increase in septal spiking ratio (MWS/SWS) upon stimulation. The importance of the loss of functional segregation of barrels, versus septa is revealed by cumulative temporal decoding analysis, supporting the notion that SST+ interneuron-mediated inhibition contributes to temporal encoding and stimulus integration. Finally, viral tracing combined with whole brain clearing and imaging reveals that barrel and septa domains project differentially to secondary somatosensory (S2) and motor (M1) cortices. These distinct projection patterns suggest that differential inhibitory processing in barrels and septa may contribute to functionally specialized downstream signaling. Together, our findings indicate that the progressive engagement of SST+ interneurons, mediated by Elfn1-dependent synaptic facilitation, underlies the preferential integration of multi-whisker stimuli in septa. This local inhibitory mechanism likely contributes to the functional segregation of barrel and septa domains and their distinct cortical projections, shaping how sensory information is processed and relayed to higher-order brain regions.

Keywords

Barrel Cortex, Elfn1 Knockout, Somatosensory Whisker Coding, Cortical Domains, Temporal Dynamics, Synaptic Integration, Sensory Projections, Progressive Functional Segregation

Introduction

Although the somatosensory whisker system is one of the principal means by which mice sense their environment and navigate the world, these tasks are carried out by a relatively small number of whiskers. This small number of vibrissae is represented in the whisker somatosensory cortex as barrel “islands” (columns) separated and surrounded by the septal “sea” (compartments), reminiscent of the whisker pad pattern on a rodent’s face, where sparse hair follicles are separated by spaces between them. In contrast, other sensory systems, such as the auditory and the visual ones, have densely packed

anatomical receptor configurations and cortical representations. Although all sensory cortices are composed of canonical microcircuits (Douglas and Martin, 2004) that include similar populations of excitatory and inhibitory neurons, maintaining segregated individual whisker information may require anatomical specializations, the barrel and septa domains. These domains may therefore create a distinct spatiotemporal stimulus representation and information coding in the barrel cortex, different from the other sensory modalities. In the adult murine barrel cortex, thalamocortical inputs coming from the ventro-postero-medial (VPM) and postero-medial (PoM) nuclei segregate into the barrel and septa domains, respectively (Alloway, 2008; Bureau et al., 2006; Kim and Ebner, 1999; Staiger and Petersen, 2021). Further, in mice (Audette et al., 2018; Sato and Svoboda, 2010; Shepherd and Svoboda, 2005) and rats (Alloway, 2008; Chakrabarti and Alloway, 2006; Melzer et al., 2006b) it was shown that information processing and flow within and from these domains target anatomically distinct sensory and motor areas. It has been suggested that the primary whisker somatosensory cortex (wS1) sends higher dimensional information needed for object recognition to the secondary somatosensory cortex (wS2), while the projections to the primary motor cortex (M1) carry less complex information that does not require segregated streams of information coming from individual whiskers (Alloway, 2008; Brecht and Sakmann, 2002; Cai et al., 2022; Sato and Svoboda, 2010). This divergence in information processing is also found within the barrel- and septa-related circuits. While barrel circuits are more involved in processing spatiotemporal whisker-object interactions, the septal circuits are more sensitive to the frequency of whisker movements, which suggests the use of temporal versus rate coding of information in barrel and septa, respectively (Melzer et al., 2006a, 2006b). Hence the existence of the septal column separating the barrels may provide mice with the means to separate these two interconnected yet very distinct information-processing routes along the temporal domain, and to make sense of their somatosensory environment through repeated sampling via cloistered information streams. Recent studies in mice have shown that barrel and septa compartments are not only anatomically segregated in terms of cell-type specific thalamocortical projections and differential expression of different genetic markers (Young et al., 2023) but also in their tuning upon single- and multi- whisker stimulation (Wang et al. 2022).

In both rats and mice, the operational identity of barrels and septa has often been attributed to the parallel bottom-up thalamocortical pathways of VPM and PoM. Here, by performing *in-vivo* silicon probe recordings simultaneously in the barrel and septa domains upon repeated single- and multi- whisker stimulation in wS1 of mice, we first show and characterize the temporal divergence between these domains. Utilizing genetic fate-mapping, passive tissue clearing, and light-sheet microscopy, we reveal that cortical somatostatin (SST+) and vasoactive intestinal peptide (VIP+) expressing interneurons show a layer-dependent differential distribution in the barrel versus septa columns. Through two-photon calcium imaging of these two populations, we show a differential engagement of SST+ cells upon multi- vs. single-whisker stimulation. By altering the short-term synaptic dynamics of incoming excitation onto these interneurons through the removal of the trans-synaptic protein Elfn1 (Elfn1 KO), we find that the domain-specific contrast ratio between multi- over single- whisker response to a repetitive stimulus is diminished. Through a progressive decoding analysis, we find that in contrast to control, whisker stimulation-evoked Elfn1 KO responses in different domains cannot be decoded efficiently. Finally, using *in-vivo* retrograde viral-based tracing, we show a layer-specific projection preference between these domains and downstream regions wS2 and M1. Hence, in addition to the anatomical specialization through thalamocortical pathways, we reveal a key contribution of local lateral cortical inhibition, provided by SST+ interneurons, in setting up the functional segregation of barrel and septa domains, and subsequently, their downstream targets.

Results

Barrel and Septa columns display differentially adaptive spiking upon repeated single- and multi- whisker stimulation

To characterize the temporal stimulus-response profiles of barrel and septal domains simultaneously, we performed *in-vivo* multi-shank (8x8) silicon probe recordings under urethane-induced light anesthesia from mouse somatosensory whisker barrel cortex (wS1), after the age of active whisking onset, postnatal day (P)20-30. Whisker stimulation was performed on either just one principal whisker (single-whisker stimulus or SWS) or via both the principal whisker and most of the macro vibrissae together (multi-whisker

stimulus or MWS; see methods) (Figure 1A). Single- or multi- whisker evoked activity within identified regions was recorded upon a 2s-long stimulation at 10Hz, similar to the average frequency at which mice actively whisk (Carvell and Simons, 1990; Grant et al., 2012). Each mouse received both stimulation paradigms. Current source density (CSD) analysis was used to assess the location of each silicon probe shank, which was later verified by post-hoc histology. The recorded activity was assigned to the stimulated principal barrel column (B), the adjacent septal column (S), or the adjacent unstimulated neighboring barrel column (N) according to SWS paradigm (Figure 1B and Supp Figure 1A to D). An example probe assignment can be seen in Supp Figure 1E. While this distinctive experimental paradigm is relatively low throughput, it has allowed us to investigate all three of these domains simultaneously. The septal compartments in mouse barrel cortex are quite narrow (Bureau et al., 2006; Sato et al., 2007) and there is the possibility of rotational misalignment during the insertion of silicon probes into the brain (Supp. Figure 1F). For these reasons we restricted our analysis of *in-vivo* responses upon SWS and MWS between barrel and septa responses to upper layers and L4, for which we have higher confidence about the anatomical domain allocation after our histological (Supp. Figure 1B) and CSD analysis (Supp. Figure 1C and D). In line with this domain allocation, t-distributed stochastic neighbor embedding (t-SNE) analysis of the multi-unit activity (MUA) recorded across the entire train of stimuli in the different domains revealed that the spiking responses between the principal barrel and the neighboring one form two separate clusters, while the responses recorded in the septa lay in between (Figure 1C; see methods).

It has previously been shown that electrophysiological responses upon whisking-based object detection saturate rapidly after a single whisker touch, while object localization may require multiple repeated whisker touches (O'Connor et al., 2013; Pammer et al., 2013). Correspondingly, when a single whisker is stimulated repeatedly, the response to the first pulse is principally bottom-up thalamic-driven responses, while the later pulses in the train are expected to also gradually engage cortico-thalamo-cortical and cortico-cortical loops (Kyriazi and Simons, 1993; Middleton et al., 2010; Russo et al., 2025). We therefore first tested whether the leading pulses of the stimulus train evoked differential responses among the principal barrel, the adjacent septa, and the neighboring barrel upon SWS and

157 MWS. For easier visualization and full appreciation of the data, we present our findings
158 both in classical time series firing-rate plot and stimulation pulse aligned stacked images
159 (Supp. Figure 2A and B, 200ms baseline followed by 2000ms evoked response to 20
160 pulses at 10Hz reshaped to 20 stacked 100ms-long evoked response image, left to right).
161 Earlier studies that separately recorded whisker-evoked responses from either barrel or
162 septa domains in rat reported that the responses of barrel neurons to single principal
163 whisker stimulation are much higher than those evoked in the septal neurons (Armstrong-
164 James and Fox, 1987; Brecht and Sakmann, 2002). The analysis of the data we obtained
165 from the simultaneous recordings at these domains in the mouse do not reveal such
166 differences in the first two stimulus responses in L4 upon single whisker stimulation
167 (SWS) (Figure 1D and 1E; white represents no significance). However, response
168 differences emerged from the 3rd pulse onward upon SWS (Figure 1E). Similar differences
169 also emerged between stimulated principal and unstimulated neighboring barrel columns
170 upon SWS (starting from 4th pulse, Figure1E, Barrel-vs-Neighbor (BN) row). Interestingly,
171 an inverted pattern of significance appeared between septa and adjacent unstimulated
172 neighboring barrels (Figure 1E, Septa-vs-Neighbor (SN) row). Additionally, repeated-
173 measures ANOVA (rmANOVA) analysis revealed that a significant main effect of
174 Condition ($F(2, 38) = 18.322$, $p < 0.001$) and a significant Condition-Time interaction
175 ($F(38, 722) = 14.618$, $p < 0.001$), indicating robust differences in overall responses and
176 their temporal dynamics across the conditions upon SWS. When multiple whiskers
177 (MWS) were activated simultaneously, like SWS, a divergence between barrel and septa
178 domain activity also occurred in Layer 4 from the 2nd pulse onward (Figure 1F and 1G).
179 However, while, rmANOVA revealed a significant main effect of Condition ($F(1, 21) =$
180 25.666, $p < 0.001$), it showed a non-significant Condition-Time interaction ($F(19, 399) =$
181 1.9076, $p = 0.13229$), indicating robust overall differences in activity between the
182 conditions, but no significant variation in their temporal patterns across the 20 time points.
183 Finally, when we calculated the response ratio upon MW over SW stimulation, we saw
184 that the septal MW/SW ratio diverged from barrel MW/SW ratio over the course of
185 repeated stimulation (Figure 1H and 1I), indicating a role of septal neurons in the
186 progressive processing MW information. This result was later confirmed by rmANOVA,
187 which revealed a significant main effect of Condition ($F(1, 21) = 5.6399$, $p = 0.027162$)

188 and a significant Condition-Time interaction ($F(19, 399) = 4.9023$, $p = 0.011313$),
189 supporting differences in overall responses and their temporal dynamics between the
190 conditions. Post-hoc tests confirmed significant differences between the multi/single
191 rations of Barrel and Septa data at multiple time points (e.g., $p < 0.0025$ at times 3, 4, 6,
192 7, 8, 10, 11, 12, 16, 19 after Bonferroni posthoc correction).
193
194 **Barrel and Septa columns display differential SST+ and VIP+ neuron densities**
195 It is known that barrel and septa domains receive different thalamic projections, from VPM
196 and PoM respectively, that might affect stimulus response properties (Ahissar et al., 2001;
197 Chmielowska et al., 1989; Koralek et al., 1988; Sosnik et al., 2001). Our
198 electrophysiological experiments show a significant divergence of responses between
199 domains upon both SWS and MWS in L4. We hypothesized that this late divergence
200 might be driven by differences in the local circuitry, and specifically inhibitory cells. We
201 therefore next assessed the spatial distribution of two inhibitory cell populations that could
202 provide distinct regulation of cortical activity in the temporal domain: SST+ and VIP+ cells.
203 Earlier research examining the three largest inhibitory neuron populations in the mouse
204 barrel cortex showed that, while parvalbumin positive (PV+) cells do not show any
205 differential density preference between barrel and septa columns, SST+ and VIP+ cells
206 have higher density in the septa in L4 (Almási et al., 2019). We attempted to verify the
207 reported differential SST+ and VIP+ neuronal distributions using an alternative imaging
208 and counting strategy. To label the two neuronal populations, we crossed the SST-Cre
209 and VIP-Cre lines with a tdTomato reporter mouse line (Ai14). To comprehensively
210 quantify the density of SST+ and VIP+ cells in the barrel and septa domains in 3D, we
211 utilized a passive CLARITY-based tissue clearing protocol, followed by light-sheet
212 microscopy using a custom-built light-sheet microscope (Vladimirov et al., 2023; Voigt et
213 al., 2019) (Figure 2A). The individual barrels in wS1 were reliably detected using auto-
214 fluorescence from the tissue acquired with a 488nm laser. tdTomato positive SST+ or
215 VIP+ neurons were detected by a 561nm laser, allowing us to accurately localize and
216 count cells in barrel and septal domains (Figure 2B and C). By adjusting the angle of each
217 barrel column in 3D (using Imaris, RRID:SCR_007370), we precisely identified the
218 column, using the barrel borders for every plane (XY, YZ, XZ) in L4 (Figure 2B, also see

219 Methods). Given that the depth of L4 can be reliably measured due to its well-defined
220 barrel boundaries, and that the relative widths of other layers have been previously
221 characterized (El-Boustani et al., 2018), we estimated laminar boundaries proportionally.
222 Specifically, Layer 2/3 was set to approximately 1.3–1.5 times the width of L4, Layer 5a
223 to ~0.5 times, and Layer 5b to a similar width as L4. Assuming isotropic tissue expansion
224 across the cortical column (Ueda et al., 2020), we extrapolated the remaining laminar
225 thicknesses proportionally. Once the columns were accurately determined, we counted
226 the number of tdTomato positive neurons in the barrels and septa and corresponding
227 volumes for density estimation. Despite their opposite distributions and neuronal density
228 changes along the depth of wS1 (Figure 2B and C), we found that both SST+ (Figure 2D)
229 and VIP+ (Figure 2E) neuronal densities were higher in L4 septa compared to barrels,
230 but we detected no difference in L2/3 and L5.
231 These results confirmed that SST+ and VIP+ interneurons have higher densities in septa
232 compared to barrels in L4 and suggest these interneurons may play a role in diverging
233 responses between barrels and septa.
234
235 **SST+ neurons are more strongly activated by multi- versus single-whisker**
236 **stimulation**
237 Having identified spatial distribution patterns of SST+ or VIP+ interneurons that could
238 contribute to the single- vs multi- whisker response scaling observed in Figure 1F; we
239 sought to assess these interneurons' response profiles upon similar whisker stimulation
240 paradigms. Therefore, we performed similar SWS and MWS experiments using acute in-
241 vivo two-photon calcium (Ca2+) imaging under light anesthesia after weaning (P21–41)
242 (Figure 3A and B). We injected OGB-1, the membrane-permeable AM-ester form of the
243 calcium indicator, into wS1 of animals expressing tdTomato in either VIP+ or SST+ INs
244 (VIPCre-Ai14 and SSTCre-Ai14 lines, respectively) to localize VIP+ and SST+ activity
245 (Figure 3A). Two-photon Ca2+ imaging was performed upon stimulation of either the C2
246 whisker at 10Hz for 2s (SWS) or most of the macro vibrissae including C2 (MWS) (Figure
247 3B). We found that both SST+ and VIP+ interneurons increased their firing upon SWS
248 (Figure 3C and D) as has been reported previously (Kastli et al., 2020), but only SST+
249 interneurons changed their firing significantly between single- and multi- whisker

250 stimulation at 10-Hz (Figure 3D, SW vs MW comparison). Although these optical
251 recordings were performed in layer 2/3 (L2/3) rather than layer 4 (L4) due to depth
252 limitations, the similarity of the peak MW/SW ratios of L2/3 populations in putative barrel
253 and septa columns (c.f. Figure 1F and Supp. Figure 3) provides support for the validity of
254 using L2/3 data to infer respective L4 cell activity. This result suggested that temporal
255 ratio differences specific to barrels and septa might involve differential activation of SST+
256 interneurons rather than VIP+ interneurons.
257
258 **Progressive multi- over single-whisker response divergence in septal populations**
259 **is abolished in Elfn1 KO mice**
260 Building on prior evidence that Elfn1 knockout disrupts short-term facilitation in SST+
261 interneurons (Sylwestrak and Ghosh, 2012; Tomioka et al., 2014; Stachniak et al., 2019,
262 2023), we attribute the abolished barrel-septa divergence in Elfn1 KO mice to altered
263 SST+ synaptic dynamics, though direct synaptic measurements were not performed here.
264 SST+ interneurons in the cortex are known to show distinct short-term synaptic plasticity,
265 particularly strong facilitation of excitatory inputs, which enables them to regulate the
266 temporal dynamics of cortical circuits (Grier et al., 2023; Liguz-Lecznar et al., 2016). This
267 facilitation allows SST+ cells to progressively enhance their inhibitory influence in
268 response to repeated stimulation, a property critical for shaping network activity. A key
269 regulator of this plasticity is the synaptic protein Elfn1, which mediates short-term synaptic
270 facilitation of excitation on SST+ interneurons (Sylwestrak and Ghosh, 2012; Tomioka et
271 al., 2014).
272 Having identified SST+ cells as potential regulators of temporal MW/SW ratio divergence,
273 we investigated how the absence of Elfn1 alters sensory-driven activity in vivo, potentially
274 shaping septal function in MW/SW response scaling. Using the same whisker stimulation
275 paradigms and domain-assignment strategy as in WT animals (Figure 1A and B; and
276 Supp. Figure 1), we recorded from barrel and septa domains in Elfn1 KO mice under both
277 single-whisker stimulation (SWS) and multi-whisker stimulation (MWS) conditions.
278 Unsupervised t-SNE analysis revealed that the domain-specific clustering of responses
279 seen in WT (Figure 1C) mice was disrupted in Elfn1 KO mice, with barrel and septa
280 responses intermingling (Figure 4A). This convergence was also evident in stimulus-

aligned stacked images, where the distinct differences between barrels and septa under SWS were largely abolished in the KO (Figure 4B, C). This was reflected in the ANOVA results, which showed a non-significant main effect of Condition ($F(2, 26) = 1.76$, $p = 0.192$) but a significant Condition-Time interaction ($F(38, 494) = 10.26$, $p < 0.001$), indicating that although the overall activity levels were similar, the temporal dynamics differed across conditions. The only remaining distinction in the KO was between directly stimulated barrels and neighboring barrels, which persisted (Figure 4B, C, Barrel-vs-Neighbor row). Interestingly, although paired analysis showed that the temporal divergence between barrel and septal domains observed in WT Layer 4 was diminished in Elfn1 KO mice (Figure 4D, E), rmANOVA revealed that both the main effect of Condition ($F(1, 16) = 13.39$, $p = 0.0021$) and the Condition-Time interaction ($F(19, 304) = 6.50$, $p = 0.00034$) were significant—unlike the corresponding MWS data in wild-type animals. However, the progressive increase in the MW/SW response ratio seen in septal neurons of WT mice was absent in KO mice (Figure 4F, G, paired test), with rmANOVA showing a non-significant main effect of Condition ($F(1, 16) = 0.22$, $p = 0.647$) and a non-significant Condition × Time interaction ($F(19, 304) = 1.17$, $p = 0.281$). These results together indicate that the barrel–septum difference observed in WT animals was lost in the Elfn1 KO.

These findings suggest that in WT animals, activity spillover from principal barrels is normally constrained by the progressive engagement of SST+ interneurons, driven by Elfn1-dependent facilitation at their excitatory synapses. In the absence of Elfn1, this local inhibitory mechanism is disrupted, leading to a loss of the distinct temporal response divergence between barrel and septa domains.

Barrel and Septa response decoding identity is lost in Elfn1 KO mice

Based on our observation that Elfn1 is essential for sustaining barrel-septa response divergence, we sought to quantify how sensory information accumulates and is integrated over time in these domains—and how this process is altered in Elfn1 KO mice.

To investigate this, we performed an accumulative temporal decoding analysis using neural responses to 20 pulses of either single-whisker stimulation (SWS) or multi-whisker stimulation (MWS) at 10 Hz for 2 seconds. We segmented the response window into three

312 time ranges to identify the temporal segments driving divergence between domains: the
313 full response window (1-95ms), the first part (1-50ms) which includes the first peak, and
314 the late part (51-95ms), which includes the second firing peak (Figure 5A). A one-versus-
315 all error-correcting output code (ECOC) classifier, using a GentleBoost ensemble of
316 decision trees (Allwein et al., 2001; Friedman et al., 2000), was trained on firing profiles
317 from WT barrel, septa, and neighboring barrel domains (3-class classification for SWS)
318 or barrel and septa domains (2-class classification for MWS). We conducted 10-fold
319 cross-validation within WT and KO datasets (WT CrossVal and KO CrossVal) and tested
320 a WT-trained classifier on Elfn1 KO responses (WT Train - KO Test) to evaluate decoding
321 performance across accumulated pulses (see Methods).
322 In WT mice, decoding accuracy increased progressively with the number of pulses upon
323 SWS (Figure 5B, red) reflecting accumulated segregation of sensory information over
324 time. This SWS WT CrossVal trend was more pronounced in the first response window
325 (1-50ms) (Figure 5C vs 5D, red), indicating that domain-specific information accumulates
326 predominantly in first temporal segments in repeated single whisker sampling. Cross-
327 validation within the WT dataset (WT CrossVal) showed higher accuracy compared to the
328 WT-trained classifier tested on KO responses (WT Train - KO Test) and KO CrossVal at
329 this first segment, but not in the second (Figure 5B-D). Elfn1 KO dataset showed higher
330 cross validation performance at the second part of the response profiles (Figure 5D)
331 indicating a temporal information delay under the reduced progressive inhibition. While
332 decoding curves started at similar initial levels for SWS data (Figures 5B-D, first pulse
333 number), initial MW decoding accuracies were remarkably different (Figures 5E-G). In
334 WT mice, while the decoding accuracy increased progressively as in SWS (Figure 5E,
335 red), the difference between accumulated 20th and the starting (1st) accuracies were lower
336 than KO CrossVal results (Figures 5E-G, red vs blue) which was predominantly due to
337 the first part of the signal (Figure 5F vs 5G).
338 To assess whether stimulus representations generalize between single-whisker
339 stimulation (SWS) and multi-whisker stimulation (MWS), we trained ECOC classifiers
340 (GentleBoost) on MWS responses and tested them on SWS data, evaluating decoding
341 accuracy for barrel and septal compartments in layer 4 (L4) of the barrel cortex (Supp.
342 Fig. 4A–C). Over the full response window (1–95ms; Supp. Fig. 4A), both WT and KO

343 animals showed high generalization, with septal accuracy reaching 1.0 by pulse 6 in WT
344 and pulse 8 in KO. Septal accuracy was higher in WT (e.g., 0.8167 vs. 0.7679 for barrels
345 at pulse 1), while in KO, barrels initially led (0.8000 vs. 0.7571 at pulse 1) before septa
346 surpassed by pulse 4 (0.9214 vs. 0.9182).In the early epoch (1–50ms; Supp. Fig. 4B),
347 WT septal accuracy was slightly higher (0.7556 vs. 0.7143 for barrels at pulse 1),
348 converging to 1.0 by pulse 8. In KO, barrel accuracy exceeded septa at pulse 1 (0.8045
349 vs. 0.7500), but septa reached 1.0 by pulse 10, while barrels plateaued at 0.9955. In the
350 later epoch (51–95ms; Supp. Fig. 4C), septal accuracy surpassed barrels in both
351 genotypes (WT: 0.9944 vs. 0.9214; KO: 0.9714 vs. 0.9227 at pulse 20), with the
352 advantage evident from pulse 1 (WT: 0.7389 vs. 0.6286; KO: 0.6357 vs. 0.6364) and
353 growing with pulses.
354 These findings indicate that septa process SWS and MWS differently, with higher
355 decoding accuracy reflecting distinct, posterior medial nucleus (POm)-driven MWS
356 responses compared to minimal SWS activation. Barrels, driven by consistent ventral
357 posteromedial nucleus (VPM) input, show less distinctiveness, yielding lower accuracy.
358 In Elfn1 KO mice, the initial barrel advantage (1–50ms) suggests reduced early septal
359 distinctiveness due to disrupted excitatory drive to somatostatin-positive (SST+)
360 interneurons, with recovery in later pulses indicating compensatory mechanisms. Calcium
361 imaging confirms stronger SST+ interneuron activation in septa during MWS, driving late-
362 phase (51–95ms) response differences amplified by successive pulses. These results
363 highlight Elfn1's role in temporal integration, where SST+ interneurons enhance septal
364 MWS processing, maintaining functional segregation between domains.
365

366 **wS1 Barrel Columns and Septal Domains have different wS2 and M1 Layer-**
367 **dependent projection preferences**

368 We identified that temporal MW/SW response divergence in septal populations is
369 abolished in Elfn1 KO mice. Given that barrel and septal compartments differentially
370 process sensory input over time, this raises the question of how these distinct streams of
371 information are relayed to downstream regions and whether they contribute to separate
372 functional pathways. Following up from this observation, we finally aimed to explore if the
373 projection targets of these two wS1 domains are distinct, in a similar manner to what has

374 been revealed for visual cortex domain projections (Meier et al., 2021). Previously, it has
375 been shown that cortical pyramidal neurons in wS1 exhibit distinct long-range projection
376 patterns and sensory tuning properties depending on their projection target (S2 or M1).
377 S2-projecting pyramidal neurons tend to have narrower receptive fields, are more likely
378 to be tuned to the columnar whisker and carry more precise sensory information about
379 whisker deflections. In contrast, M1-projecting pyramidal neurons are more broadly tuned,
380 integrating information from multiple whiskers, which aligns with their role in sensorimotor
381 integration and behavior (Sato and Svoboda, 2010; Yamashita et al., 2013). This data
382 could be suggestive of distinct localization of the different projection neurons in the
383 different wS1 domains. By utilizing *in vivo* retrograde AAV injections in two of the main
384 target cortical regions of wS1, we aimed to characterize the projections from wS1 to wS2
385 and M1.
386 We injected a retrograde AAV virus expressing GFP in wS2 or M1 in separate adult mice
387 and dissected the brains 4 weeks after the injection (Figure 6A). We utilized again the
388 passive CLARITY-based tissue clearing and imaged the whole brain using mesoSPIM.
389 The auto-fluorescence of the barrels allowed for labeling of barrel columns in 3D (Figure
390 6B). With the same strategy as our previous analysis on interneuron population
391 distributions (Figure 2), we counted the number of neurons in wS1 barrel and septa
392 domains across the cortical layers (Figure 6C) and measured the corresponding domain
393 volumes to estimate projection densities as a proxy for connectivity levels between S1-
394 S2 and S1-M1.
395 As an internal control and in line with expectations, fewer projections arose from layer 4
396 barrels to either wS2 or M1 than from other cortical layers (Figure 6C and D). However,
397 more neurons in septa between mid-L4 and upper-L5B sent wS2 projections (Figure 6D,
398 left, turquois), and more neurons in septa from L3 to L4 project to M1, compared to the
399 neurons in barrels (Figure 6D, right, magenta). Additionally, a secondary comparative
400 analysis showed that barrels in L3 host significantly more wS2-projecting-neurons (Figure
401 6E, left, purple), while L5A septal domains host significantly more M1-projecting neurons
402 (Figure 6E, right, magenta). This differential targeting suggests that the temporal whisker-
403 evoked processing specialization of barrel and septa domains may shape how distinct

streams of sensory information are conveyed to higher-order cortical areas, potentially influencing perceptual processing in wS2 and sensorimotor integration in M1.

Discussion

In the absence of visual stimuli, humans explore objects through tactile interactions, where the initial touch begins the process of information accumulation, with subsequent touches refining the identification and characterization of the object. Rodents rely on a similar strategy during active whisking, where sequential whisker contacts allow for the progressive refinement of object recognition and spatial mapping (Armstrong-James and Fox, 1987; Kheradpezhouh et al., 2017; Petersen, 2007). This process involves parallel ascending pathways that transmit peripheral touch sensations to the cortex, with the primary somatosensory cortex mapping whisker spatial patterns directly onto cortical barrels, and in between spaces, septa (Van Der Loos and Woolsey, 1973; Woolsey et al., 1975).

Our study reveals that the functional segregation between barrel and septa domains in the mouse whisker primary somatosensory cortex (wS1) is not only anatomically defined by distinct thalamocortical projections but is also dynamically shaped by local inhibitory circuits, particularly those involving somatostatin-positive (SST+) interneurons. Through a combination of functional and anatomical techniques, we show that the temporal divergence in spiking activity between barrel and septa domains is mediated by the short-term synaptic facilitation properties of SST+ interneurons and are critically dependent on the synaptic protein Elfn1. Furthermore, using a decoder we show that this temporal divergence may affect the integration of sensory information during repeated whisker stimulation, which may be subsequently routed to differential downstream cortical areas, such as the secondary somatosensory cortex (wS2) and primary motor cortex (M1).

Among the inhibitory neuron classes, SST+ interneurons are known for their high spontaneous activity and powerful regulation of local neural networks through dense feedback connections onto nearby pyramidal neurons (Urban-Ciecko and Barth, 2016). In contrast, VIP+ interneurons influence network function through a disinhibitory circuit, inhibiting SST+ (and to a lesser extent PV+) interneurons upon activation, which in turn reduces inhibition on pyramidal cells (Karnani et al., 2016; Lee et al., 2013; Pi et al., 2013).

Thus SST+ interneurons may contribute to barrel-septal identity using surround inhibition, while being regulated themselves by VIP+ interneuron activity under certain behaviorally relevant sensory-motor tasks. Additionally, fast-spiking (FS) interneurons, predominantly PV+ cells, form a distinct network electrically coupled with other FS cells and are preferentially activated by thalamocortical inputs, providing rapid feedforward inhibition that complements the slower, facilitating inhibition of SST+ networks (Gibson et al., 1999). Our analysis of SST+ cell distribution, shows a higher density in the septa in L4, compared to barrels. Interestingly, layer 4 SST+ interneuron axons remain within layer 4 (Xu et al., 2013) in the somatosensory cortex, unlike SST+ of layers 2/3 and 5/6 which are Martinotti type and target layer 1. In addition, while Martinotti cells receive facilitating synapses from pyramidal cells and form inhibitory synapses onto dendrites of neighboring pyramidal cells (Silberberg and Markram, 2007), non-Martinotti SST cells strongly inhibit fast spiking cells, but also stellate cells in layer 4 (Ma et al., 2006; Xu et al., 2013). During naturalistic whisking, SST+ and PV+ cells show divergent activation patterns, with FS cells showing transient excitation due to rapid synaptic depression, while SST+ cells show the opposite (Tan et al., 2008). These divergent dynamics are consistent with the presence of two parallel inhibitory networks in layer 4, where FS (PV+) cells exhibit strong short-term depression and LTS (SST+) cells display facilitation, enabling differential recruitment by temporal patterns of activity (Beierlein et al., 2003). It is currently unclear though under which behavioral circumstances SST+ cells of L4 would engage in inhibition of excitatory cells versus inhibition of PV+ cells. Our data suggest that under our experimental conditions, a bottom-up activation paradigm, SST+ cells overall engage in the progressive inhibition of the local L4 circuit, rather than disinhibition. Although we interpret divergence in L2/3 responses as potentially inherited from L4 dynamics, direct laminar recordings and manipulation would be required to confirm this. We propose that the divergence in MWS/SWS ratios across barrel and septal domains reflects dynamic microcircuit interactions, not fully or solely captured in SST+ density. Barrel domains, dominated by VPM inputs, engage PV+ and SST+ neurons to stabilize responses, with Elfn1-dependent facilitation gradually increasing inhibition during repetitive SWS. Septal domains, receiving facilitating POm inputs and having a higher L4 SST+ density, show progressive inhibitory buildup that amplifies the MWS/SWS ratio. Trans-laminar and lateral SST+

projections likely propagate these dynamics to L2/3, explaining divergence despite uniform SST+ density. Direct laminar cell-type specific and VPM/POm-specific optogenetic manipulations will be critical to test this model.

To assess whether temporal divergence in spiking carries meaningful sensory information, we conducted a detailed accumulative temporal decoding analysis. We find that in wild-type mice, decoding accuracy for SWS increased progressively with each additional pulse, particularly in the initial response window (1-50ms), indicating that domain-specific information accumulates primarily in early temporal segments during repeated whisker sampling. This progressive accumulation of decodable information was severely disrupted in Elfn1 KO mice, with cross-validation showing significantly reduced performance compared to wild-type, especially in early response segments. Interestingly, Elfn1 KO mice showed higher cross-validation performance in the later response segment (51-95ms), suggesting a temporal delay in information processing due to reduced progressive inhibition. Under multi-whisker stimulation, wild-type and knockout mice showed markedly different initial decoding accuracies, with the difference between accumulated and initial accuracies being lower in wild-type than in Elfn1 KO mice. Even though we have made significant efforts to define the columns in the barrel cortex, we are aware that the CLARITY-based passive clearing protocol leads to tissue expansion. In addition, different barrel columns were analyzed across different brains due to the technical difficulties, adding a small variability to the dataset. Regardless, in toto our anatomical connectivity mapping would suggest that disruption in temporal information processing in the two domains is crucial for maintaining the functional segregation of parallel processing streams to wS2 and M1.

The differential projection patterns of barrel and septa domains to wS2 and M1 further suggest that the temporal processing capabilities of these domains influence how sensory information is integrated with motor output. For example, the projection of septa domains to M1 may facilitate the rapid translation of sensory information into motor commands, while the projection of barrel domains to wS2 may support more detailed sensory discrimination. This pathway-specific modulation is supported by evidence of learning-related plasticity in S1 cortico-cortical neurons, where M1-projecting neurons encode kinematic features and are involved in touch-related activity, while S2-projecting neurons

enhance discrimination of trial types and decision-related patterns (Chen et al., 2015). Additionally, the preferential activation of inhibitory interneurons, such as SST+ neurons, by thalamocortical inputs—due to stronger excitatory synapses—underpins the initial processing stages in the barrel cortex (Cruikshank et al., 2007). The disruption of the informational integrity of these projections in Elfn1 KO mice could therefore have significant implications for sensorimotor integration and behavior, potentially impairing the adaptive plasticity observed in wild-type animals during task learning.

It is important to note that while our study focuses on the mouse barrel cortex, there are significant differences between rodent species, such as rats and mice, in terms of cortical organization and whisker system function. Most research on whisker stimulation had traditionally focused on rats (Estebanez et al., 2016; Petersen, 2007; Roy et al., 2011; Tanke et al., 2018). The existence of septa in the mouse barrel cortex has been debated, with some suggesting that the distinction between barrel and septal circuits is less pronounced in mice compared to rats (Bureau et al., 2006; Sato et al., 2007). For example, the mouse barrel cortex has fewer neurons per column and thinner septa compared to rats, which may influence the degree of functional segregation between barrel and septa domains. While many animals have whiskers, only a subset of animals have visible cortical barrels. For instance, cats have whiskers and brainstem barrelettes but lack cortical barrels (Nomura et al., 1986; Rice, 1985; Rice et al., 1985). Interestingly, the presence of barrels in the cortex seems to correlate with volitional whisking behavior, underlining the importance of one-to-one mapping for processing individual whisker information. Our findings show that septa are crucial in separating these parallel whisker streams by modulating the lateral cortico-cortical information flow during repetitive whisker touches. Our data support this modulation being significantly influenced by the short-term facilitation properties of synaptic inputs onto SST+ interneurons, facilitated by the Elfn1 gene, alongside distinct bottom-up inputs to each domain. The loss of temporal segregation in Elfn1 KO mice could hinder object recognition, which relies on multi-whisker integration in septa, while sparing simpler detection tasks mediated by barrels.

Although Elfn1 is constitutively knocked out, this and earlier studies have found that barrel structure is preserved (Stachniak et al., 2023, 2019). Further, the distribution of Elfn1 expressing interneurons is not different in KO mice, suggesting minimal developmental

disruption (Dolan and Mitchell, 2013). Nonetheless, we acknowledge that subtle circuit changes cannot be ruled out without the usage of time-depended conditional knockout of the gene.

In summary, our study demonstrates that there exists a functional segregation of barrel and septa domains in the mouse whisker somatosensory cortex, and that it is dynamically shaped by the temporal dynamics of SST+ interneuron activity, imparted by the synaptic protein Elfn1. This temporal divergence is essential for the integration of sensory information over repeated whisker deflections and for the differential projection-dependent information processing in downstream cortical areas. These findings highlight the importance of local inhibitory circuits in shaping cortical processing and offer new insights into mechanisms underlying sensory perception and behavior.

Acknowledgments

We thank members of the Karayannis lab for suggestions and comments on the manuscript. Authors also thank George Kanatouris for helping with animal handling and breeding.

Funding

This work was supported by Swiss National Science Foundation Grant S-41260-01-01 (T.K) and European Research Council Grant 679175 (T.K).

Author Contributions

A.Ö.A. curated the data, analyzed in-vivo silicon probe recordings and the two-photon calcium imaging data, performed the decoder analysis and wrote the manuscript. T.J.S. conceptualized the study, maintained Elfn1 KO line, performed earlier electrophysiological characterizations and contributed to the drafting of the manuscript, J.W.Y. performed silicon probe recordings, AvdB collected two-photon calcium imaging data, L.C. performed AAV virus injection, tissue clearing and light-sheet data acquisition and analysis, R.K. performed tissue clearing and light-sheet image acquisition, T.K. conceptualized and supervised the study and wrote the manuscript.

559 **Declaration of Interest**

560 The authors declare no competing interests.

561

562 **Methods**

563

564 RESOURCE AVAILABILITY

565 Lead Contact

566 Further information and requests for resources and reagents should be directed to the
567 Lead Contact, T.K. (karayannis@hifo.uzh.ch)

568

569 Materials Availability

570 This study did not generate new unique reagents.

571 Data and Code Availability

572 The datasets and analysis routines are available from the first author on reasonable
573 request.

574

575 **Mice**

576 All the animal experiments followed the guidelines of the Veterinary Office of Switzerland
577 and were approved by the Cantonal Veterinary Office Zurich and the University of Zurich.
578 husbandry with a 12-h reverse dark-light cycle (7 a.m. to 7 p.m. dark) at 24 °C and variable
579 humidity. Adult (5- to 10-week-old) male C57BL6J wide type mice were used for
580 retrograde tracing. Animal lines used in this study are VIP-IRES-Cre
581 (Vip$^{tm1(cre)Zjh}$/J)(Taniguchi et al., 2011), SST-IRES-Cre (Sst$^{tm2.1(cre)Zjh}$/J) (Taniguchi et al.,
582 2011), Ai14 (B6;129S6-Gt(ROSA)26Sor$^{tm14(CAG-tdTomato)Hze}$/J)(Madisen et al., 2010) and
583 Elfn1 KO (Elfn1tm1(KOMP)Vlcg). Both male and female mice were used in all
584 experiments.

585

586 **In-Vivo Silicon Probe Recording**

587 We used 4 Elfn1 KO and 4 WT littermates at the age of P20 to P30 for the multi-electrode
588 silicon probe recordings. Mice were under urethane induced anesthesia (1.5g/1kg)
589 throughout the experiment. A heating pad was used to maintain the mouse's body

590 temperature at 37°C. The depth of anesthesia was checked with breathing speed and
591 paw reflexes throughout the experiment. The skull of the right hemisphere was exposed
592 by removing the skin on top, and a metallic head holder was implanted on the skull with
593 cyanoacrylate glue and dental cement. A 26G needle was used to open a ~2mm x 2mm
594 cranial window which exposed the S1 barrel field (wS1). Extreme care was taken not to
595 cause damage or surface bleeding during surgery.
596 wS1 neural activities were recorded with an 8-shank-64-channel silicon probe. Each of
597 the 8 shanks has 8 recording sites (100μm apart). The distance between each shank is
598 200μm (A8x8-Edge-5mm-100-200-177-A64, NeuroNexus Technologies, Ann Arbor, MI,
599 USA). The silicon probe was labeled with DiI (1,1′-dioctadecyl-3,3,3′,3′-
600 tetramethylindocarbocyanine, Molecular Probes, Eugene, OR, USA) and inserted
601 perpendicularly into the barrel cortex. A silver wire was placed into the cerebellum as a
602 ground electrode. All data were acquired at 20 kHz and stored with MC Rack
603 (RRID:SCR_014955) software (Multi Channel systems). The total duration of multi-
604 electrode recordings varied between 3 to 5 hours. After each experiment, the animal was
605 deeply anesthetized by ketamine (120 mg/kg, ketamine, 50 mg/mL, HamelnPharma,
606 Hameln Germany) and perfused through the aorta with ringer solution. The brain was
607 kept in 4% PFA. Tangential sections (200-μm thick) were prepared for vesicular glutamate
608 transporter 2 (vGlut2, Synaptic Systems, 135404; 1:1000) immunohistochemistry. By
609 combining the DiI and vGlut2 staining, the insertion position of the 8 shank probes was
610 identified in the barrel cortex. DiI marks contained within the vGlut2 staining were defined
611 as barrel recordings, while DiI marks outside vGlut2 staining were septal recordings.
612
613 **Whisker Stimulation**
614 Either a single principal whisker (SW, single whisker) or multiple whiskers (MW, multi
615 whisker) were stimulated 1mm from the snout in rostral-to caudal direction (about 1mm
616 displacement) using a stainless-steel rod (1 mm diameter) connected to a miniature
617 solenoid actuator. The movement of the tip of the stimulator bar was measured precisely
618 using a laser micrometer (MX series, Metralight, CA, USA) with a 2500 Hz sampling rate.
619 The stimulus takes 26ms to reach the maximal 1 mm whisker displacement, with a total
620 duration of 60ms until it reaches baseline (Yang et al., 2017). Both SW and MW

621 stimulation was performed at 10Hz for 2s and each stimulation repeated for 20 times (20
622 Trials). The inter-trial interval was 30s. In every experiment, multiple whiskers were singly
623 stimulated to increase the probability of finding a proximal barrel-septa and neighboring
624 barrel triplets. We first performed multi-whisker stimulation and at the end individual single
625 whisker stimulations. Individual whisker stimulation was performed by attaching a pipet
626 tip to the stimulator, which was then placed in contact with the principal whisker under a
627 dissecting stereoscope. We trimmed the whiskers where necessary, to avoid them
628 touching each other and to avoid stimulating multiple whiskers. By putting the pipette tip
629 very close (almost touching) to the principal whisker, the movement of the tip (limited to
630 1mm) reliably moved the principal whisker, as observed under the stereoscope. MW
631 stimulation was performed by contacting multiple whiskers with 1cm-wide masking tape
632 attached to the pipet tip.
633
634 **In vivo two-photon calcium imaging**
635 Neuronal ensembles in superficial layers of the principal whisker barrel field mapped by
636 intrinsic signal imaging were bolus-loaded with the AM ester form of Oregon Green
637 BAPTA-1 by pressure injection (OGB-1; 1 mM solution in Ca^{2+}-free Ringer's solution; 2-
638 min injection at 150–200 µm depth) as described previously (Stosiek et al., 2003). The
639 craniotomy was then filled with agarose (type III-A, 1% in Ringer's solution; Sigma) and
640 covered with an immobilized glass plate. Two-photon Ca^{2+} imaging was performed with
641 a Scientifica HyperScope two-photon laser scanning microscope one hour after bolus
642 loading using a Ti:sapphire laser system at 900 nm excitation (Coherent Chameleon;
643 ~120 femtosecond laser pulses). Two-channel fluorescence images of 256 × 128 pixels
644 at 11.25 Hz (HyperScope galvo-mode) were collected with a 16x water-immersion
645 objective lens (Nikon, NA 0.8). In all, 3–5 separate spots have been imaged per animal.
646 Per imaging spot, 10 trials of 20s-long evoked activity recorded for each of single- and
647 multi- whisker stimulation paradigms. Data acquisition was controlled by ScanImage
648 (RRID:SCR_014307) (Pologruto et al., 2003).
649
650
651

652 **Analysis of calcium imaging data**

653 Ca^{2+} imaging data is analyzed using custom MATLAB scripts. First, fluorescence image
654 time-series for a given region were concatenated. The concatenated data was then
655 aligned using a Fourier domain cross-correlation based subpixel registration algorithm
656 (Guizar-Sicairos et al., 2008) to correct for translational drift (registered on red tdTomato
657 channel and transferred to OGB-1 channel). Average intensity projections of the imaging
658 data were used as reference images to manually annotate regions of interest (ROIs)
659 corresponding to individual neurons. Neurons with somata partly out-of-focus were not
660 included. Ca^{2+} signals were expressed as the mean pixel value of the relative
661 fluorescence change $\Delta F/F = (F-F_0)/F_0$ in each given ROI. F_0 was calculated as the bottom
662 5% of the fluorescence trace. Neuropil patches surrounding each neuron is defined by all
663 pixels not assigned to a neuronal soma or astrocyte of the corresponding neuron ROI
664 annotation (Peron et al., 2015) (A disk shaped region around the neuron of interest with
665 excluding any intersecting neighboring neuronal ROI). Neuropil correction is performed
666 as $F_{corrected} = F_{neuron} - \alpha * F_{neuropil}$. α is estimated for each imaging spot separately using the
667 formula $F_{blood_vessel}/F_{surrounding_neuropil}$ (Kerlin et al., 2010). For each stimulus, the evoked
668 responses of 10 trials were analyzed and the response magnitude expressed as the mean
669 of the evoked $\Delta F/F$ integral (%·s; integral of the first 2s response starting at stimulus
670 onset).

671

672 **Analysis of Silicon Probe Data**

673 Extracellular silicon probe data were analyzed using a custom-made Matlab script
674 (MATLAB (RRID:SCR_001622), Version: 2024a, MathWorks, MA, USA). The raw data
675 signal was band-pass filtered (0.8-5 kHz), and the multi-unit activity (MUA) was extracted
676 with the threshold of 7.5 times the standard deviation (SD) of baseline (Yang et al., 2017).
677 The current source density (CSD) map was used to identify laminar probe contact
678 location. The earliest CSD sink was identified as layer 4, followed by L2-3 (Reyes-Puerta
679 et al., 2015; Van Der Bourg et al., 2017). Post hoc histology was then performed on plane-
680 aligned brain sections which would allow us to detect barrels and septa, so as to confirm
681 the insertion domains of each recorded shank. Layer specificity of each electrode could
682 therefore not be confirmed by histology as we did not have coronal sections in which to

683 measure electrode depth. Instead, the recording sites above the one in L4 were
684 designated as 2/3 and the ones below as deeper layer ones. The analysis of the MUA
685 activity was smoothed using a Gaussian kernel (0 mean, 5ms sigma) and used for also
686 delineating the different layers.
687 The Area Under the Curve (AUC) was computed as the integral of the smoothed firing
688 rate (spikes per millisecond) over a 50ms window following each whisker stimulation
689 pulse, using trapezoidal integration. Firing rate data for layer 4 barrel and septal regions
690 in wild-type (WT) and knockout (KO) mice were smoothed with a 3-point moving average
691 and averaged across blocks of 20 trials. Plotted values represent the percentage ratio of
692 multi-whisker (MW) to single whisker (SW) AUC with error bars showing the standard
693 error of the mean. Each data point reflects the mean AUC ratio for a stimulation pulse
694 across approximately 11 blocks (220 trials total). The y-axis indicates percentages.
695
696 **Decoder Analysis**
697 Recordings from the principal barrel, adjacent septa, and a neighboring unstimulated
698 barrel were organized into three matrices for wild-type (WT) animals: a 280 × 95 × 20
699 matrix for the stimulated barrel (14 Barrels, 95ms, 20 pulses), a 180 × 95 × 20 matrix for
700 the septa (9 Septa, 95ms, 20 pulses), and a 360 × 95 × 20 matrix for the neighboring
701 barrel (18 Neighboring barrels, 95ms, 20 pulses). For Elfn1-KO animals: 11-barrel
702 columns, 7 septal columns, 11 unstimulated neighbors from N=4 mice.
703 Each matrix's dimensions correspond to the number of recording channels, time points
704 (95ms epochs), and 20 individual stimulation trials, respectively. Although each trial
705 originally spanned 2000ms (20 pulses at 10Hz), the analysis focused on the first 95ms
706 post-stimulation (95ms instead of 100ms). To examine the impact of different temporal
707 windows on classification performance, three versions of the analysis were performed by
708 varying the time-range parameter, 1 to 95ms for the full epoch, 1 to 50ms for the first part,
709 and 51 to 95ms for the second part.
710 For each stimulation trial, data was accumulated pulse-by-pulse. In each iteration
711 (ranging from 1 to 20), the corresponding segments from the three matrices were
712 reshaped into two-dimensional feature matrices by concatenating the selected time points

across the accumulated pulses. Labels were then assigned to the reshaped data (‘B’ for the barrel, ‘S’ for septa, and ‘N’ for the neighboring barrel).

We employed a classification approach utilizing error-correcting output codes (ECOC) models with a gentle adaptive boosting (GentleBoost) strategy to train classifiers. This method is particularly effective in handling imbalanced data and unequal misclassification costs. Like Logit Boost, each weak learner in the ensemble fitted a regression model to response values, $y_n \in \{-1, +1\}$. The mean-squared error is computed as:

$$N \sum_{n=0}^{d} d(t)_n \left(y_n - h_t(x_n)\right)^2$$

where $d(t)_n$ represents observation weights at step t (summing up to 1) and $h_t(x_n)$ denotes predictions from the regression model h_t fitted to response values y_n. As the strength of individual learners diminishes, the weighted mean-squared error converges towards 1.

Three distinct evaluations were performed. WT-to-KO Prediction, the ECOC classifier trained on WT data (compiled from the three regions) was used to predict labels from corresponding recordings in knockout (KO) mice. Within-Group Cross-Validation (WT), A cross-validation procedure was applied to the WT dataset using MATLAB’s *crossval* function to assess classifier performance internally. Within-Group Cross-Validation (KO), Similarly, an ECOC classifier was trained and cross-validated on the KO dataset.

For each evaluation, confusion matrices were generated and summary accuracy statistics computed. Accuracy was tracked as a function of the number of accumulated pulses (from 1 to 20). The accuracy value represents the overall classification accuracy, defined as the proportion of correctly predicted samples across all classes. Specifically, it is calculated as the sum of true positives (TP) for all classes obtained from the trace of the confusion matrix (i.e., the diagonal elements where predicted and actual labels match) divided by the total number of samples. The formula used is:

Accuracy = trace(confusionMat) / totalSamples

, where totalSamples is the sum of all entries in the confusion matrix.

This metric reflects the overall correctness of the classifier and is naturally constrained between 0 and 1. The function first constructs the confusion matrix confusionMat, where rows represent actual classes and columns represent predicted classes, either by

743 computing it from labels using MATLAB's confusionmat or using a precomputed matrix.
744 The number of classes is determined from the matrix dimensions, and the total number
745 of samples is the sum of all matrix entries. For each class, the function calculates TP
746 (correct predictions for that class), TN (correct predictions for all other classes), FP (false
747 positives for that class), and FN (false negatives for that class) by manipulating the
748 confusion matrix.
749 To characterize the evolution of classification accuracy with increasing pulse number,
750 non-linear exponential functions of the form:

751 $$f(x) = a - b * \exp(-cx)$$

752 were fitted to the accuracy data using a non-linear least squares approach (implemented
753 via the *fminspleas* function). Separate fits were obtained for the WT-to-KO prediction, WT
754 cross-validation, and KO cross-validation accuracy curves. The fitted curves and raw
755 accuracy data were then plotted. This integrated analysis pipeline allowed for systematic
756 comparison of classification performance across spatial locations and conditions and an
757 assessment of the temporal dynamics underlying the neural responses to single-whisker
758 stimulation. The same strategy has been used for multi-whisker decoding but between
759 only Barrel and Septa.
760

761 **Retrograde tracing**

762 Mice aged from P10-37 were anesthetized by isoflurane and a small craniotomy was
763 made above the injection site (M1 or S2). 200nl retrograde AAV virus, ssAAV-retro/2-
764 CAG-EGFP-WPRE-SV40p(A) (physical titer: $5x10^{12}$ vg/ml) was injected 200-500μm deep
765 in the M1 or S2. Virus was purchased from Zurich Viral Vector Facility (Cat#: V24-retro).
766 During the retrograde virus injection, the location of M1 and S2 injections was determined
767 by stereotaxic coordinates (Yamashita et al., 2018). After acquiring the light-sheet
768 images, we were able to post hoc examine the injection site in 3D and confirm that the
769 injections were successful in targeting the regions intended. Although it would have been
770 informative to do so, we did not functionally determine the whisker-related M1 and
771 whisker-related S2 region in this experiment.
772
773

774 **Tissue Processing for Passive Clearing and Imaging**

775 The method used for hydrogel-based tissue clearing is explained in detail elsewhere
776 (Chung and Deisseroth, 2013). Briefly, Mice age P29-70 (4 weeks after retrograde AAV
777 virus injection) or SST-Ai14 and VIP-Ai14 mice age from P14-77 were transcardially
778 perfused using 1x PBS and Hydrogel solution (1% PFA, 4% Acrylamide, 0.05% Bis). The
779 collected brains were post-fixed for 48 h in a Hydrogel solution (1% PFA, 4% Acrylamide,
780 0.05% Bis). Afterward, the Hydrogel polymerization was induced at 37 °C. Following the
781 polymerization, the brains were immersed in 40 mL of 8% SDS and kept shaking at room
782 temperature until the tissue was cleared sufficiently (15-90 days depending on the
783 animal's age). Finally, after 2–4 washes in PBS, the brains were put into a self-made
784 refractive index matching solution (RIMS). They were left to equilibrate in 5 mL of RIMS
785 for at least 4 days at RT (Room Temperature) before being imaged. After clearing, brains
786 were attached to a small weight and loaded into a quartz cuvette, then submerged in
787 RIMS, and imaged using a home-built mesoscale selective plane illumination microscope
788 (mesoSPIM, Voigt et al., 2019). The microscope consists of a dual-sided excitation path
789 using a fiber-coupled multiline laser combiner (405, 488, 515, 561, 594, 647 nm, Omicron
790 SOLE-6) and a detection path comprising an Olympus MVX-10 zoom macroscope with a
791 1× objective (Olympus MVPLAPO 1x), a filter wheel (Ludl 96A350), and a scientific CMOS
792 (sCMOS) camera (Hamamatsu Orca Flash 4.0 V3). For imaging tdTomato and eGFP a
793 561 nm excitation with a 594 long-pass filter and 488 nm & 520/35 (BrightLine HC, AHF)
794 were used, respectively. The excitation paths also contain galvo scanners (GCM-2280-
795 1500, Citizen Chiba) for light-sheet generation and reduction of streaking artifacts due to
796 absorption of the light-sheet. In addition, the beam waist is scanning using electrically
797 tunable lenses (ETL, Optotune EL-16-40-5D-TC-L) synchronized with the rolling shutter
798 of the sCMOS camera. This axially scanned light-sheet mode (ASLM) leads to a uniform
799 axial resolution across the field-of-view of 5–10 μm (depending on zoom and wavelength).
800 The magnification 0.8X (pixel size: 8.23 μm) was used for the view of the whole brain and
801 2X (pixel size: 3.26 μm) was used for the view of barrel cortex. Further technical details
802 of the mesoSPIM are described elsewhere (Vladimirov et al., 2023; Voigt et al., 2019).
803
804

805 **Analysis of cleared brain imaging data**

806 Barrel cortex was imaged in 3D with 2X objective. The images were processed through
807 Fiji and Imaris to visualize the 3D structure of the barrel cortex. XY-, YZ-, XZ- projections
808 were visualized in Imaris, which allows us to adjust the correct angle for each barrel
809 column to be vertical against XY-plane. This method allowed us identify barrel and septa
810 in layers 2-3 and 5 and layer 4. In addition, the depth information is also precisely acquired
811 for each barrel column. SST+ or VIP+ neuron numbers, S2-projected and M1-projected
812 S1 neuron numbers were counted in icy. Max projection for each 50 ums along barrel
813 columns was acquired and neurons on each max projection image were counted
814 automatically by icy (RRID:SCR_010587) with the same threshold for all the brains. Each
815 barrel was drawn according to the barrel map from each brain by max projection. The
816 area of septa was calculated by subtracting the whole selected area from all the selected
817 barrel areas.

818

819 **t-SNE Analysis**

820 To visualize the segregation of neural responses across the different cortical domains,
821 we applied t-distributed Stochastic Neighbor Embedding (t-SNE) to the averaged
822 datasets. t-SNE was used to reduce the high-dimensional data into a 2D space for
823 visualization. The parameters for t-SNE were set to use the *barneshut* algorithm for
824 efficiency, with a perplexity of 9 and exaggeration of 3 to enhance cluster separation. The
825 resulting t-SNE coordinates were plotted using MATLAB's *gscatter* function to distinguish
826 between the different domains (Barrel, Septa, Neighboring). This analysis allowed us to
827 visually inspect the clustering of neural responses from different cortical domains.

828 In summary, each point in the t-SNE plots represents an averaged response across 20
829 trials for a specific domain (barrel, septa, or neighbor) and genotype (WT or KO), with
830 approximately 14 points per domain derived from the 280 trials in each dataset. The input
831 features are preprocessed by averaging blocks of 20 trials into 1900-dimensional vectors
832 (95ms × 20), which are then reduced to 2D using t-SNE with the specified parameters.
833 This approach effectively highlights the segregation and clustering patterns of neural
834 responses across cortical domains in both WT and KO conditions.

835

836 **Statistical Analysis of the Multi-Unit Activity**

837 To evaluate the statistical significance of differences in multi-unit activity (MUA)
838 responses between barrel (B), septa (S), and neighboring barrel (N) domains across 20
839 pulses of whisker stimulation, we performed a pulse-by-pulse comparison using the non-
840 parametric Mann-Whitney U test (also known as the Wilcoxon rank-sum test). This
841 analysis was conducted on the averaged MUA data recorded from Layer 4 of the whisker
842 somatosensory cortex (wS1) in wild-type (WT) and Elfn1 knockout (KO) mice during
843 single-whisker stimulation (SWS) and multi-whisker stimulation (MWS) paradigms, as
844 detailed above. For each of the 20 stimulation pulses (1 to 20), the MUA data for each
845 domain were reshaped and averaged across trials. The Mann-Whitney U test was then
846 applied pairwise to assess differences between domains: barrel vs. septa (B vs S), barrel
847 vs. neighboring barrel (B vs N), and septa vs. neighboring barrel (S vs N). The resulting
848 p-values were stored in a 3×20 matrix, where rows correspond to the pairwise
849 comparisons and columns represent the pulse number. To visualize the statistical
850 outcomes, a heatmap was generated using MATLAB (Version 2024a, MathWorks, MA,
851 USA). A custom discrete colormap was created by adapting the hot colormap, which
852 originally provides a gradient of 10 colors ranging from black (low values) to white (high
853 values). We selected specific indices from this gradient (10, 8, 6, 4, 2, 1) to define a 10-
854 level discrete colormap, assigning the darkest shade (black) to p-values ≤ 0.05 (indicating
855 statistical significance) and progressively lighter shades to higher p-values, with the
856 lightest shade (white) representing p-values > 0.05. The colormap was inverted to ensure
857 that significant p-values (≤ 0.05) appeared as light shades against a dark background,
858 enhancing visual contrast. The heatmap was plotted with p-values scaled between 0 and
859 0.05, using the custom colormap.

860

861 **Statistical Analysis**

862 Data are represented as mean ± SEM unless stated otherwise. Statistical comparisons
863 have been done using a one-tailed Mann-Whitney-U test for non-paired data and one-
864 tailed Wilcoxon signed-rank test for paired comparisons (the statistical significance
865 threshold was set to $p<0.05$; in the Figures, different degrees of evidence against the null
866 hypothesis are indicated by asterisks ($p<0.05$: *; $p<0.01$: **; $p<0.001$: ***). Cell densities

867 in Figures 2 and 6 were compared using repeated measures ANOVA. All tests were
868 conducted using custom codes in Matlab.
869
870 **Figure Legends**
871 **Figure 1.** Temporal divergences emerge between barrel and septa domains upon
872 repeated whisker stimulation in Layer 4 of mouse wS1. (A) Either the principal whisker
873 (SWS, or single whisker) or most of the whiskers (MWS, or multi whisker) were stimulated
874 for 2s at 10Hz (20 pulses) for 20 times (20 trials). (B) Acute simultaneous *in-vivo* silicon
875 probe (8x8) recordings were performed from barrel and septa domains (>P21) (C) t-SNE
876 analysis of the average firing dynamics from three domains after averaging 20 single
877 trials. (D) Left: Average multi-unit firing profiles recorded at Layer 4 of barrel (black),
878 unstimulated neighbor (blue) and septa (pink) columns upon 2s-long 10Hz repeated
879 single whisker stimulation. Right: Pulse-aligned firing heatmap of the SWS data. Color
880 scale bar represents spikes per millisecond. (E) Pair-wise statistical comparisons of first
881 50ms of the single whisker responses from barrel (B), septa (S) and neighbor (N) for each
882 pulse (Mann-Whitney-U-Test). (F) Left: Average multi-unit firing profiles recorded at Layer
883 4 of barrel (black) and septa (pink) columns upon 2s-long 10Hz repeated multi whisker
884 stimulation. Right: Pulse-aligned firing heatmap of the MWS data. Color scale bar
885 represents spikes per millisecond. (G) Pair-wise statistical comparisons of first 50ms of
886 the multi whisker responses from barrel (B) and septa (S) for the 1st, 2nd,3rd and 20th
887 pulses (Mann-Whitney-U-Test). (H) Temporal ratio dynamics (average AUC MW
888 responses divided by average AUC SW responses) for barrel and septa. (I) statistical
889 comparison of average AUC ratios of all pulses (1-20), average of the first six (1-6) or
890 average of the last 14 pulses (7-20), respectively. (p values are color coded in E, stars
891 represent *: $p<0.05$; **: $p<0.01$; ***: $p<0.001$ in G and I.)
892
893 **Figure 2.** SST+ and VIP+ neuron densities differ at Barrel and Septa Domains in Layer
894 4. (A) A passive CLARITY-based tissue clearing protocol was performed on the collected
895 brains which were subsequently imaged in their entirety using a custom-built light-sheet
896 microscope (mesoSPIM). 561nm wavelength was used to image tdTomato, 488nm
897 wavelength was used to image autofluorescence. (B) 3D reconstruction of cleared SST-

898 Ai14 (left) and VIP-Ai14 (right) barrel cortex. X-Y, X-Z and Y-Z views are presented
899 focusing with a single barrel max projection. The brain was rotated to achieve the
900 orientation that the barrel columns are perpendicular to the X-Y view. The scale bars are
901 set for 500µm. (C) Max projection examples of SST (red) and VIP (blue) neurons in wS1
902 L2-3, L4 and L5. Quantified barrels (yellow lines) and septa (green lines) are circled out
903 which are perpendicular to X-Y (top-down) view. The scale bar is set for 200µm. (D) SST+
904 neuron density distribution over laminae for barrel and septal domains (N=4 mice, n=54
905 Barrels and surrounding septa per barrel). Normalized cell densities plotted as a function
906 of depth. 0µm represents the top of layer 4. SST+ interneuron density is significantly
907 higher in septa (p=0.0015, F=30.64, repeated-measures ANOVA). (E) VIP+ neuron
908 density distribution over laminae for barrel and septal domains. (N=4 mice, n=53 Barrels
909 and surrounding septa per barrel). Normalized cell densities plotted as a function of depth.
910 0µm represents the top of layer 4. VIP+ interneuron density is also significantly higher in
911 septa (p=0.021, F=9.63, repeated-measures ANOVA).
912
913 **Figure 3**. Single- vs multi- whisker responses of SST+ and VIP+ Interneurons (A)
914 Interneurons are labeled with tdTomato using reporter mouse lines and Ca^{2+} imaging has
915 been performed after bulk loading of OGB-1. scale bar 35µm. (B) Schematic
916 representation of the single- and multi- whisker stimulation protocol upon 10Hz
917 stimulation. (C) Δ*F/F* traces of evoked activity of SST (on top) and VIP (on bottom)
918 interneurons (*N* = 3 animals per group, VIP P21+: 138 cells, SST P21+: 51 cells). (D) Area
919 under the curve (AUC) of the first 2s of the Δ*F/F* traces of all SST and VIP cells upon
920 single- (SW: 2s-long principal whisker evoked activity) and multi- whisker (MW: 2s-long
921 multi whisker stimulation evoked activity) stimulation (Wilcoxon signed-rank test,
922 Baseline: 2s-long baseline activity).
923
924 **Figure 4.** Loss of Elfn1 abolishes barrel-septa response divergences upon single-whisker
925 stimulation. (A) t-SNE analysis of the average firing dynamics from three domains. (B)
926 Left: Average multi-unit firing profiles recorded at Layer 4 of barrel (gray), unstimulated
927 neighbor (light blue) and septa (purple) columns (11-barrel columns, 7 septal columns,
928 11 unstimulated neighbors from N=4 mice) upon 2s-long 10Hz repeated single whisker

929 stimulation. Right: Pulse-aligned firing heatmap of the same data by representing each
930 stimulation pulse response on one row. Color scale bar represents spikes per millisecond.
931 (C) Pair-wise statistical comparisons of first 50ms of the single whisker responses from
932 barrel (B), septa (S) and neighbor (N) for each pulse (Mann-Whitney-U-Test). (D) Left:
933 Average KO multi-unit firing profiles recorded at Layer 4 of barrel (gray) and septa
934 (magenta) columns upon 2s-long 10Hz repeated multi whisker stimulation. Right: Pulse-
935 aligned firing heatmap of the KO MWS data. Color scale bar represents spikes per
936 millisecond. (E) Pair-wise statistical comparisons of first 50ms of the multi whisker
937 responses from barrel (B) and septa (S) for the 1st, 2nd,3rd and 20th pulses (Mann-Whitney-
938 U-Test). (F) Temporal ratio dynamics (average AUC KO MW responses divided by
939 average AUC KO SW responses) for barrel and septa. (G) statistical comparison of
940 average AUC ratios of all pulses (1-20), average of the first six (1-6) or average of the last
941 14 pulses (7-20), respectively. (p values are color coded in C, stars represent **: $p<0.01$
942 in E.)
943
944 **Figure 5.** Accumulative decoding analysis shows an alteration of columnar domain
945 identity in Elfn1 KO animals. (A) For the decoding analysis, the entire pulse response,
946 only the first 50ms or only the last 45ms has been used. (B) Decoder analysis of the full
947 pulse response profiles in L4 upon SWS. (C) Decoder analysis of the first part of the pulse
948 response (1-50ms) profiles in L4 upon SWS. (D) Decoder analysis of the second part of
949 the pulse response (51-95ms) profiles in L4 upon SWS. (E) Decoder analysis of the full
950 pulse response profiles in L4 upon MWS. (F) Decoder analysis of the first part of the pulse
951 response (1-50ms) profiles in L4 upon MWS (G) Decoder analysis of the second part of
952 the pulse response (51-95ms) profiles in L4 upon MWS.
953
954 **Figure 6.** wS1 barrel and septa columns differentially project to wS2 and M1 (A) The
955 schematics of the experimental protocol. The retro-AAV-CAG-GFP was injected in either
956 S2, or M1 at P20-30 and the brains were dissected 4 weeks after the virus injection
957 following the tissue clearing and whole brain imaging. (B) 3D reconstruction of the cleared
958 brain with S2(Left panels) or M1(right panels) injection. X-Y, X-Z and Y-Z views are
959 presented focus with a single barrel max projection. The brain was rotated to achieve the

960 orientation that the septa is perpendicular to the X-Y view (top-down). Scale bars in whole
961 brain view are set for 2000um and the scale bars in X-Y, X-Z and Y-Z views are set for
962 200um. (C) Max projection examples of S2-projected wS1 neurons and M1-projected
963 wS1 neurons in L2-3, L4 and L5 in barrel vs septa. Quantified barrels (yellow lines) and
964 septa (blue lines) are circled out which are perpendicular to X-Y (top-down) view. Scale
965 bars are set for 200um. (D) Left: Normalized cell density profiles of S2 projection neurons
966 at barrel and septa columns. 0μm represents the top of layer 4. L4 and L5a septa columns
967 send significantly more projections to S2 than barrel column (N=4 mice) (p=0.0139,
968 F=11.79, repeated-measures ANOVA). Right: Normalized cell density profiles of M1
969 projections neurons at barrel and septa columns. 0μm represents the top of layer 4. L3
970 and L4 septa columns send significantly more projections to M1 (N=6 mice) (p=0.0032,
971 F=14.82, repeated measures ANOVA). (E) Left: Normalized cell density profiles of S2
972 and M1 projection neurons at barrel columns. 0μm represents the top of L4. L3 barrel
973 columns send significantly more projections to S2 (N=4 mice with S2 injections, N=6 mice
974 with M1 injections) (p=0.0293, F=7.02, repeated-measures ANOVA). Right: Normalized
975 cell density profiles of S2 and M1 projections neurons at septa columns. 0μm represents
976 the top of L4. L5a septal columns send significantly more projections to M1 N=4 mice with
977 S2 injections, N=6 mice with M1 injections) (p=0.0402, F=5.98, repeated measures
978 ANOVA).
979
980 **Supplementary Figure 1.** An example of assignment of barrel, septa and Neighbor
981 electrodes using histology and current source density (CSD) analysis. (A) Shank
982 electrode map of 8x8 silicon probes. (B) Probe locations were labeled (DiI) after each
983 experiment using histology (vGlut2 staining). Matching shank locations are indicated
984 using yellow numbers. Blue dots represent the insertion sites. The red and white text
985 depicts corresponding barrel names. (Scale bar: 250μm) (C) All whiskers are stimulated
986 one-by-one. C1 to C5 barrel responses upon single whisker stimulation are shown from
987 top to bottom. (D) A closer look on C1, C2 and C3 whisker stimulations and corresponding
988 CSD at shanks 5,6,7 and 8. (E), Barrel (B), adjacent septa (S) and the adjacent
989 neighboring barrel (N) were assigned according to the probe insertion sites and L4 barrel
990 autofluorescence in combination with CSD responses. For example, while shanks 6 and

8 show strong response upon single whisker stimulation (and hence assigned as barrels), shank 7 does not show the expected response (hence assigned as septa). Only the triplets of electrodes were used in the analysis in which principal barrel (B), adjacent septa (S) and the adjacent neighboring barrel (N) were captured by the probe insertion sites for any experiment (Left). 14-barrel columns, 9 septal columns, 18 unstimulated neighboring barrels from N=4 mice. (F) An ideal schematic representation (on the left). Realistically, we cannot always be sure if an entire shank is consistently going through a barrel or septal column due to the curvature of the cortex (on the right) for above and below of layer4.

Supplementary Figure 2. Representation of the conversion of the two-second-long single trial recordings into 20x100ms matrices. (A) Schematic representation. (B) An example data. The last 5ms of each pulse have been discarded in further analysis.

Supplementary Figure 3. (A) Left: Average multi-unit firing profiles recorded at Layer 2/3 of barrel (black), unstimulated neighbor (blue) and septa (pink) columns upon 2s-long 10Hz repeated single whisker stimulation. Right: Another representation of the same data but converted into an image by representing each stimulation pulse response on one row. (B) Left: Average multi-unit firing profiles recorded at Layer 2/3 of barrel (black), unstimulated neighbor (blue) and septa (pink) columns upon 2s-long 10Hz repeated multi whisker stimulation. Right: Another representation of the same data but converted into an image by representing each stimulation pulse response on one row. (C) Left: Temporal ratio dynamics (average AUC MW responses divided by average AUC SW responses) for barrel and septa for layer2/3. Right: statistical comparison of average AUC ratios of all pulses (1-20), first six (1-6) or last 14 pulses (7-20), respectively (stars represent *: $p<0.05$; **: $p<0.01$; ***: $p<0.001$ in F and G. Wilcoxon rank sum test).

Supplementary Figure 4. Cross-condition decoding between single-whisker (SWS) and multi-whisker stimulation (MWS). Recordings from the principal barrel and adjacent septa were organized into two matrices for two separate WT and KO decoders. To assess generalization, decoders were trained on MWS responses and tested on SWS responses.

Data were accumulated pulse-by-pulse, and in each iteration (1–20) the corresponding trial segments were concatenated across pulses to construct feature matrices. Decoding performance was computed for three temporal windows: (A) the full response (1–95ms); (B) the first epoch (1–50ms), and (C) the second epoch (51–95ms).

References

Ahissar E, Sosnik R, Bagdasarian K, Haidarliu S. 2001. Temporal frequency of whisker movement. II. Laminar organization of cortical representations. *J Neurophysiol* **86**. doi:10.1152/jn.2001.86.1.354

Alloway KD. 2008. Information processing streams in rodent barrel cortex: The differential functions of barrel and septal circuits. *Cerebral Cortex*. doi:10.1093/cercor/bhm138

Allwein EL, Schapire RE, Singer Y. 2001. Reducing multiclass to binary: A unifying approach for margin classifiers. *Journal of Machine Learning Research* **1**.

Almási Z, Dávid C, Witte M, Staiger JF. 2019. Distribution patterns of three molecularly defined classes of gabaergic neurons across columnar compartments in mouse barrel cortex. *Front Neuroanat* **13**. doi:10.3389/fnana.2019.00045

Armstrong-James M, Fox K. 1987. Spatiotemporal convergence and divergence in the rat S1 "Barrel" cortex. *Journal of Comparative Neurology* **263**. doi:10.1002/cne.902630209

Audette NJ, Urban-Ciecko J, Matsushita M, Barth AL. 2018. POm Thalamocortical Input Drives Layer-Specific Microcircuits in Somatosensory Cortex. *Cereb Cortex* **28**. doi:10.1093/cercor/bhx044

Beierlein M, Gibson JR, Connors BW. 2003. Two Dynamically Distinct Inhibitory Networks in Layer 4 of the Neocortex. *J Neurophysiol* **90**. doi:10.1152/jn.00283.2003

Brecht M, Sakmann B. 2002. Dynamic representation of whisker deflection by synaptic potentials in spiny stellate and pyramidal cells in the barrels and septa of layer 4 rat somatosensory cortex. *Journal of Physiology*. doi:10.1113/jphysiol.2002.018465

Bureau I, Von Paul F Saint, Svoboda K. 2006. Interdigitated paralemniscal and lemniscal pathways in the mouse barrel cortex. *PLoS Biol* **4**. doi:10.1371/journal.pbio.0040382

Cai L, Yang JW, Wang CF, Chou SJ, Luhmann HJ, Karayannis T. 2022. Identification of a Developmental Switch in Information Transfer between Whisker S1 and S2 Cortex in Mice. *Journal of Neuroscience* **42**. doi:10.1523/JNEUROSCI.2246-21.2022

Carvell GE, Simons DJ. 1990. Biometric analyses of vibrissal tactile discrimination in the rat. *Journal of Neuroscience* **10**. doi:10.1523/jneurosci.10-08-02638.1990

Chakrabarti S, Alloway KD. 2006. Differential origin of projections from SI barrel cortex to the whisker representations in SII and MI. *Journal of Comparative Neurology* **498**. doi:10.1002/cne.21052

Chen JL, Margolis DJ, Stankov A, Sumanovski LT, Schneider BL, Helmchen F. 2015. Pathway-specific reorganization of projection neurons in somatosensory cortex during learning. *Nat Neurosci* **18**. doi:10.1038/nn.4046

Chmielowska J, Carvell GE, Simons DJ. 1989. Spatial organization of thalamocortical and corticothalamic projection systems in the rat SmI barrel cortex. *Journal of Comparative Neurology* **285**. doi:10.1002/cne.902850304

Chung K, Deisseroth K. 2013. CLARITY for mapping the nervous system. *Nat Methods* **10**. doi:10.1038/nmeth.2481

Cruikshank SJ, Lewis TJ, Connors BW. 2007. Synaptic basis for intense thalamocortical activation of feedforward inhibitory cells in neocortex. *Nat Neurosci* **10**. doi:10.1038/nn1861

Dolan J, Mitchell KJ. 2013. Mutation of Elfn1 in mice causes seizures and hyperactivity. *PLoS One* **8**. doi:10.1371/journal.pone.0080491

Douglas RJ, Martin KAC. 2004. Neuronal circuits of the neocortex. *Annu Rev Neurosci*. doi:10.1146/annurev.neuro.27.070203.144152

El-Boustani S, Ip JPK, Breton-Provencher V, Knott GW, Okuno H, Bito H, Sur M. 2018. Locally coordinated synaptic plasticity of visual cortex neurons in vivo. *Science (1979)* **360**. doi:10.1126/science.aao0862

Estebanez L, Bertherat J, Shulz DE, Bourdieu L, Léger JF. 2016. A radial map of multi-whisker correlation selectivity in the rat barrel cortex. *Nat Commun* **7**. doi:10.1038/ncomms13528

Friedman J, Hastie T, Tibshirani R. 2000. Additive logistic regression: A statistical view of boosting. *Ann Stat*. doi:10.1214/aos/1016218223

Gibson JR, Belerlein M, Connors BW. 1999. Two networks of electrically coupled inhibitory neurons in neocortex. *Nature* **402**. doi:10.1038/47035

Grant RA, Mitchinson B, Prescott TJ. 2012. The development of whisker control in rats in relation to locomotion. *Dev Psychobiol* **54**. doi:10.1002/dev.20591

Grier BD, Parkins S, Omar J, Lee HK. 2023. Selective plasticity of fast and slow excitatory synapses on somatostatin interneurons in adult visual cortex. *Nat Commun* **14**. doi:10.1038/s41467-023-42968-y

Guizar-Sicairos M, Thurman ST, Fienup JR. 2008. Efficient subpixel image registration algorithms. *Opt Lett* **33**. doi:10.1364/ol.33.000156

Karnani MMM, Jackson J, Ayzenshtat I, Tucciarone J, Manoocheri K, Snider WGG, Yuste R. 2016. Cooperative Subnetworks of Molecularly Similar Interneurons in Mouse Neocortex. *Neuron* **90**. doi:10.1016/j.neuron.2016.02.037

Kastli R, Vighagen R, van der Bourg A, Argunsah AÖ, Iqbal A, Voigt FF, Kirschenbaum D, Aguzzi A, Helmchen F, Karayannis T. 2020. Developmental divergence of sensory stimulus representation in cortical interneurons. *Nat Commun* **11**. doi:10.1038/s41467-020-19427-z

Kerlin AM, Andermann ML, Berezovskii VK, Reid RC. 2010. Broadly Tuned Response Properties of Diverse Inhibitory Neuron Subtypes in Mouse Visual Cortex. *Neuron* **67**. doi:10.1016/j.neuron.2010.08.002

Kheradpezhouh E, Adibi M, Arabzadeh E. 2017. Response dynamics of rat barrel cortex neurons to repeated sensory stimulation. *Sci Rep* **7**. doi:10.1038/s41598-017-11477-6

Kim U, Ebner FF. 1999. Barrels and septa: Separate circuits in rat barrel field cortex. *Journal of Comparative Neurology* **408**. doi:10.1002/(SICI)1096-9861(19990614)408:4<489::AID-CNE4>3.0.CO;2-E

Koralek KA, Jensen KF, Killackey HP. 1988. Evidence for two complementary patterns of thalamic input to the rat somatosensory cortex. *Brain Res* **463**. doi:10.1016/0006-8993(88)90408-8

Kyriazi HT, Simons DJ. 1993. Thalamocortical response transformations in simulated whisker barrels. *Journal of Neuroscience* **13**. doi:10.1523/jneurosci.13-04-01601.1993

Lee S, Kruglikov I, Huang ZJ, Fishell G, Rudy B. 2013. A disinhibitory circuit mediates motor integration in the somatosensory cortex. *Nat Neurosci* **16**. doi:10.1038/nn.3544

Liguz-Lecznar M, Urban-Ciecko J, Kossut M. 2016. Somatostatin and somatostatin-containing neurons in shaping neuronal activity and plasticity. *Front Neural Circuits*. doi:10.3389/fncir.2016.00048

Ma Y, Hu H, Berrebi AS, Mathers PH, Agmon A. 2006. Distinct subtypes of somatostatin-containing neocortical interneurons revealed in transgenic mice. *Journal of Neuroscience* **26**. doi:10.1523/JNEUROSCI.0661-06.2006

Madisen L, Zwingman TA, Sunkin SM, Oh SW, Zariwala HA, Gu H, Ng LL, Palmiter RD, Hawrylycz MJ, Jones AR, Lein ES, Zeng H. 2010. A robust and high-throughput Cre reporting and characterization system for the whole mouse brain. *Nat Neurosci* **13**:133–140. doi:10.1038/nn.2467

Meier AM, Wang Q, Ji W, Ganachaud J, Burkhalter A. 2021. Modular network between postrhinal visual cortex, amygdala, and entorhinal cortex. *Journal of Neuroscience* **41**. doi:10.1523/JNEUROSCI.2185-20.2021

Melzer P, Champney GC, Maguire MJ, Ebner FF. 2006a. Rate code and temporal code for frequency of whisker stimulation in rat primary and secondary somatic sensory cortex. *Exp Brain Res* **172**:370–386. doi:10.1007/s00221-005-0334-1

Melzer P, Sachdev RNS, Jenkinson N, Ebner FF. 2006b. Stimulus frequency processing in awake rat barrel cortex. *Journal of Neuroscience* **26**. doi:10.1523/JNEUROSCI.2620-06.2006

Middleton JW, Kinnischtzke A, Simons DJ. 2010. Effects of thalamic high-frequency electrical stimulation on whisker-evoked cortical adaptation. *Exp Brain Res* **200**. doi:10.1007/s00221-009-1977-0

Nomura S, Itoh K, Sugimoto T, Yasui Y, Kamiya H, Mizuno N. 1986. Mystacial vibrissae representation within the trigeminal sensory nuclei of the cat. *Journal of Comparative Neurology* **253**. doi:10.1002/cne.902530110

O'Connor DH, Hires SA, Guo Z V., Li N, Yu J, Sun QQ, Huber D, Svoboda K. 2013. Neural coding during active somatosensation revealed using illusory touch. *Nat Neurosci* **16**. doi:10.1038/nn.3419

Pammer L, O'Connor DH, Hires SA, Clack NG, Huber D, Myers EW, Svoboda K. 2013. The mechanical variables underlying object localization along the axis of the whisker. *Journal of Neuroscience* **33**. doi:10.1523/JNEUROSCI.4316-12.2013

Peron S, Chen TW, Svoboda K. 2015. Comprehensive imaging of cortical networks. *Curr Opin Neurobiol*. doi:10.1016/j.conb.2015.03.016

Petersen CCH. 2007. The functional organization of the barrel cortex. *Neuron*. doi:10.1016/j.neuron.2007.09.017

Pi HJ, Hangya B, Kvitsiani D, Sanders JI, Huang ZJ, Kepecs A. 2013. Cortical interneurons that specialize in disinhibitory control. *Nature* **503**. doi:10.1038/nature12676

Pologruto TA, Sabatini BL, Svoboda K. 2003. ScanImage: Flexible software for operating laser scanning microscopes. *Biomed Eng Online* **2**. doi:10.1186/1475-925X-2-13

Reyes-Puerta V, Sun JJ, Kim S, Kilb W, Luhmann HJ. 2015. Laminar and Columnar Structure of Sensory-Evoked Multineuronal Spike Sequences in Adult Rat Barrel Cortex in Vivo. *Cerebral Cortex* **25**. doi:10.1093/cercor/bhu007

Rice FL. 1985. An attempt to find vibrissa-related barrels in the primary somatosensory cortex of the cat. *Neurosci Lett* **53**. doi:10.1016/0304-3940(85)90180-6

Rice FL, Gomez C, Barstow C, Burnet A, Sands P. 1985. AComparative analysis of the development of the primary somatosensory cortex: Interspecies similarities during barrel and laminar development. *Journal of Comparative Neurology* **236**. doi:10.1002/cne.902360405

Roy NC, Bessaih T, Contreras D. 2011. Comprehensive mapping of whisker-evoked responses reveals broad, sharply tuned thalamocortical input to layer 4 of barrel cortex. *J Neurophysiol* **105**. doi:10.1152/jn.00939.2010

Russo S, Claar LD, Furregoni G, Marks LC, Krishnan G, Zauli FM, Hassan G, Solbiati M, d'Orio P, Mikulan E, Sarasso S, Rosanova M, Sartori I, Bazhenov M, Pigorini A, Massimini M, Koch C, Rembado I. 2025. Thalamic feedback shapes brain responses evoked by cortical stimulation in mice and humans. *Nature Communications* **16**. doi:10.1038/s41467-025-58717-2

Sato TR, Gray NW, Mainen ZF, Svoboda K. 2007. The functional microarchitecture of the mouse barrel cortex. *PLoS Biol* **5**. doi:10.1371/journal.pbio.0050189

Sato TR, Svoboda K. 2010. The functional properties of barrel cortex neurons projecting to the primary motor cortex. *Journal of Neuroscience* **30**. doi:10.1523/JNEUROSCI.3774-09.2010

Shepherd GMG, Svoboda K. 2005. Laminar and columnar organization of ascending excitatory projections to layer 2/3 pyramidal neurons in rat barrel cortex. *Journal of Neuroscience* **25**. doi:10.1523/JNEUROSCI.1173-05.2005

Silberberg G, Markram H. 2007. Disynaptic Inhibition between Neocortical Pyramidal Cells Mediated by Martinotti Cells. *Neuron* **53**. doi:10.1016/j.neuron.2007.02.012

Sosnik R, Haidarliu S, Ahissar E. 2001. Temporal frequency of whisker movement. I. Representations in brain stem and thalamus. *J Neurophysiol* **86**. doi:10.1152/jn.2001.86.1.339

Stachniak TJ, Argunsah AÖ, Yang J-W, Cai L, Karayannis T. 2023. Presynaptic kainate receptors onto somatostatin interneurons are recruited by activity throughout development and contribute to cortical sensory adaptation. *Journal of Neuroscience* **43**. doi:10.1523/JNEUROSCI.1461-22.2023

Stachniak TJ, Kastli R, Hanley O, Argunsah AÖ, Van Der Valk EGT, Kanatouris G, Karayannis T. 2021. Postmitotic prox1 expression controls the final specification of cortical VIP interneuron subtypes. *Journal of Neuroscience* **41**. doi:10.1523/JNEUROSCI.1021-21.2021

Stachniak TJ, Sylwestrak EL, Scheiffele P, Hall BJ, Ghosh A. 2019. Elfn1-induced constitutive activation of mglur7 determines frequency-dependent recruitment of somatostatin interneurons. *Journal of Neuroscience* **39**. doi:10.1523/JNEUROSCI.2276-18.2019

Staiger JF, Petersen CCH. 2021. Neuronal circuits in barrel cortex for whisker sensory perception. *Physiol Rev* **101**. doi:10.1152/physrev.00019.2019

Stosiek C, Garaschuk O, Holthoff K, Konnerth A. 2003. In vivo two-photon calcium imaging of neuronal networks. *Proc Natl Acad Sci U S A* **100**. doi:10.1073/pnas.1232232100

Tan Z, Hu H, Huang ZJ, Agmon A. 2008. Robust but delayed thalamocortical activation of dendritic-targeting inhibitory interneurons. *Proc Natl Acad Sci U S A* **105**. doi:10.1073/pnas.0710628105

Taniguchi H, He M, Wu P, Kim S, Paik R, Sugino K, Kvitsani D, Fu Y, Lu J, Lin Y, Miyoshi G, Shima Y, Fishell G, Nelson SB, Huang ZJ. 2011. A Resource of Cre Driver Lines for Genetic Targeting of GABAergic Neurons in Cerebral Cortex. *Neuron* **71**:995–1013. doi:10.1016/j.neuron.2011.07.026

Tanke N, Borst JGG, Houweling AR. 2018. Single-cell stimulation in barrel cortex influences psychophysical detection performance. *Journal of Neuroscience* **38**. doi:10.1523/JNEUROSCI.2155-17.2018

Tomioka NH, Yasuda H, Miyamoto H, Hatayama M, Morimura N, Matsumoto Y, Suzuki T, Odagawa M, Odaka YS, Iwayama Y, Won Um J, Ko J, Inoue Y, Kaneko S, Hirose S, Yamada

K, Yoshikawa T, Yamakawa K, Aruga J. 2014. Elfn1 recruits presynaptic mGluR7 in trans and its loss results in seizures. *Nat Commun* **5**. doi:10.1038/ncomms5501

Ueda HR, Ertürk A, Chung K, Gradinaru V, Chédotal A, Tomancak P, Keller PJ. 2020. Tissue clearing and its applications in neuroscience. *Nat Rev Neurosci*. doi:10.1038/s41583-019-0250-1

Urban-Ciecko J, Barth AL. 2016. Somatostatin-expressing neurons in cortical networks. *Nat Rev Neurosci* **17**. doi:10.1038/nrn.2016.53

Van Der Bourg A, Yang JW, Reyes-Puerta V, Laurenczy B, Wieckhorst M, Stüttgen MC, Luhmann HJ, Helmchen F. 2017. Layer-Specific Refinement of Sensory Coding in Developing Mouse Barrel Cortex. *Cerebral Cortex* **27**. doi:10.1093/cercor/bhw280

Van Der Loos H, Woolsey TA. 1973. Somatosensory cortex: Structural alterations following early injury to sense organs. *Science (1979)* **179**. doi:10.1126/science.179.4071.395

Vladimirov N, Voigt F, Naert T, Araujo GR, Cai R, Reuss AM, Zhao S, Schmid P, Hildebrand S, Schaettin M, Groos D, Mateos JM, Bethge P, Yamamoto T, Aerne V, Roebroeck A, Ertürk A, Aguzzi A, Ziegler U, Stoeckli ET, Baudis L, Lienkamp SS, Helmchen F. 2023. The Benchtop mesoSPIM: a next-generation open-source light-sheet microscope for large cleared samples. *bioRxiv*.

Voigt FF, Kirschenbaum D, Platonova E, Pagès S, Campbell RAA, Kastli R, Schaettin M, Egolf L, van der Bourg A, Bethge P, Haenraets K, Frézel N, Topilko T, Perin P, Hillier D, Hildebrand S, Schueth A, Roebroeck A, Roska B, Stoeckli ET, Pizzala R, Renier N, Zeilhofer HU, Karayannis T, Ziegler U, Batti L, Holtmaat A, Lüscher C, Aguzzi A, Helmchen F. 2019. The mesoSPIM initiative: open-source light-sheet microscopes for imaging cleared tissue. *Nat Methods* **16**. doi:10.1038/s41592-019-0554-0

Wang HC, LeMessurier AM, Feldman DE. 2022. Tuning instability of non-columnar neurons in the salt-and-pepper whisker map in somatosensory cortex. *Nat Commun* **13**. doi:10.1038/s41467-022-34261-1

Woolsey TA, Welker C, Schwartz RH. 1975. Comparative anatomical studies of the Sml face cortex with special reference to the occurrence of "barrels" in layer IV. *Journal of Comparative Neurology* **164**. doi:10.1002/cne.901640107

Xu H, Jeong HY, Tremblay R, Rudy B. 2013. Neocortical Somatostatin-Expressing GABAergic Interneurons Disinhibit the Thalamorecipient Layer 4. *Neuron* **77**. doi:10.1016/j.neuron.2012.11.004

Yamashita T, Pala A, Pedrido L, Kremer Y, Welker E, Petersen CCH. 2013. Membrane potential dynamics of neocortical projection neurons driving target-specific signals. *Neuron* **80**. doi:10.1016/j.neuron.2013.10.059

Yang JW, Prouvot PH, Reyes-Puerta V, Stüttgen MC, Stroh A, Luhmann HJ. 2017. Optogenetic modulation of a minor fraction of parvalbumin-positive interneurons specifically affects spatiotemporal dynamics of spontaneous and sensory-evoked activity in mouse somatosensory cortex in vivo. *Cerebral Cortex* **27**. doi:10.1093/cercor/bhx261

Young TR, Yamamoto M, Kikuchi SS, Yoshida AC, Abe T, Inoue K, Johansen JP, Benucci A, Yoshimura Y, Shimogori T. 2023. Thalamocortical control of cell-type specificity drives circuits for processing whisker-related information in mouse barrel cortex. *Nat Commun* **14**. doi:10.1038/s41467-023-41749-x

Figures

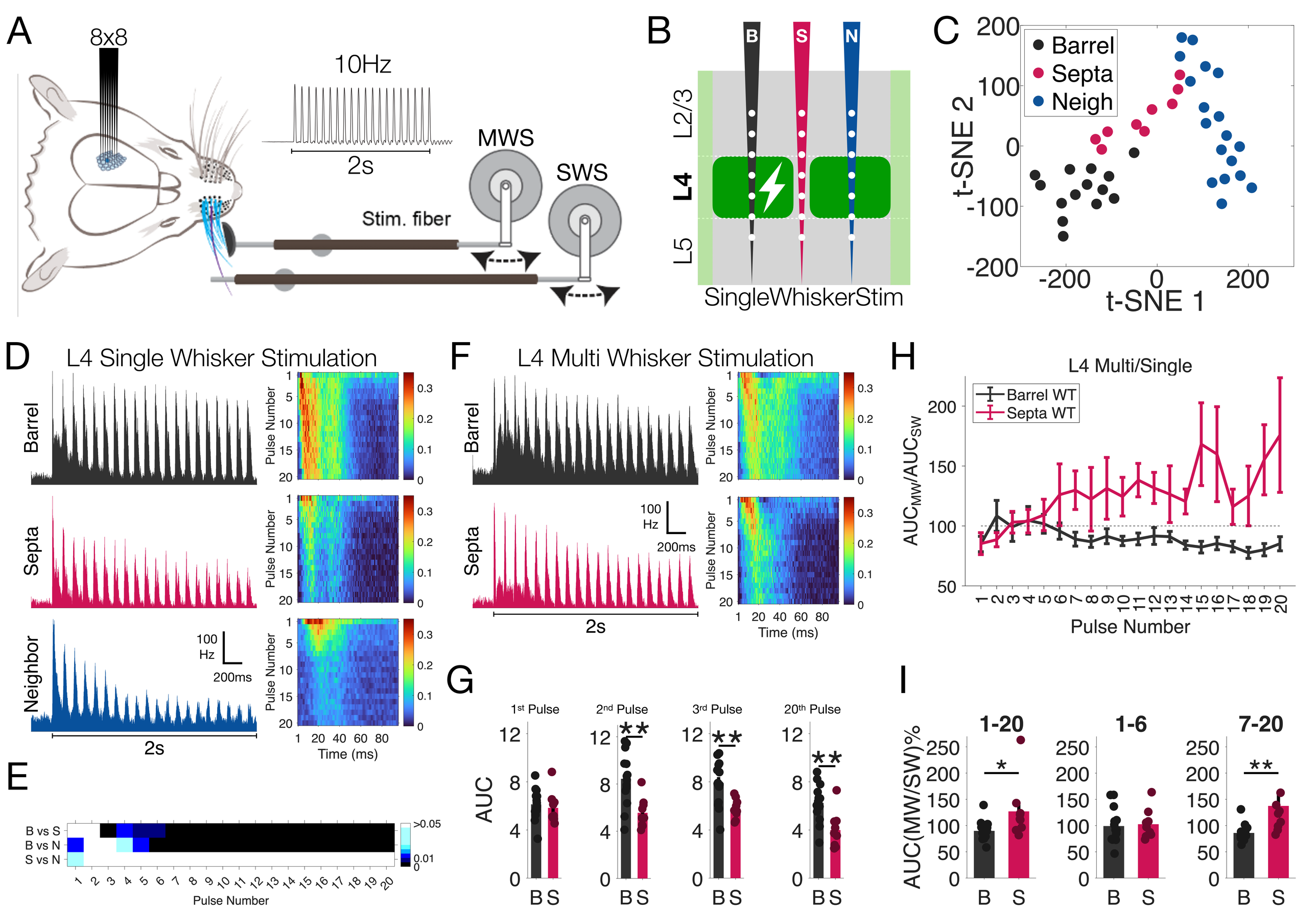
A
8x8
10Hz
2s
MWS
SWS
Stim. fiber
B
B
S
N
L2/3
L4
L5
SingleWhiskerStim
C
Barrel
Septa
Neigh
t-SNE 2
t-SNE 1
D
L4 Single Whisker Stimulation
Barrel
Septa
Neighbor
Pulse Number
100 Hz
200ms
2s
Time (ms)
F
L4 Multi Whisker Stimulation
H
L4 Multi/Single
Barrel WT
Septa WT
AUC_MW/AUC_SW
Pulse Number
E
B vs S
B vs N
S vs N
>0.05
0.01
Pulse Number
G
1st Pulse
2nd Pulse
3rd Pulse
20th Pulse
AUC
I
1-20
1-6
7-20
AUC(MW/SW)%

Figure 1

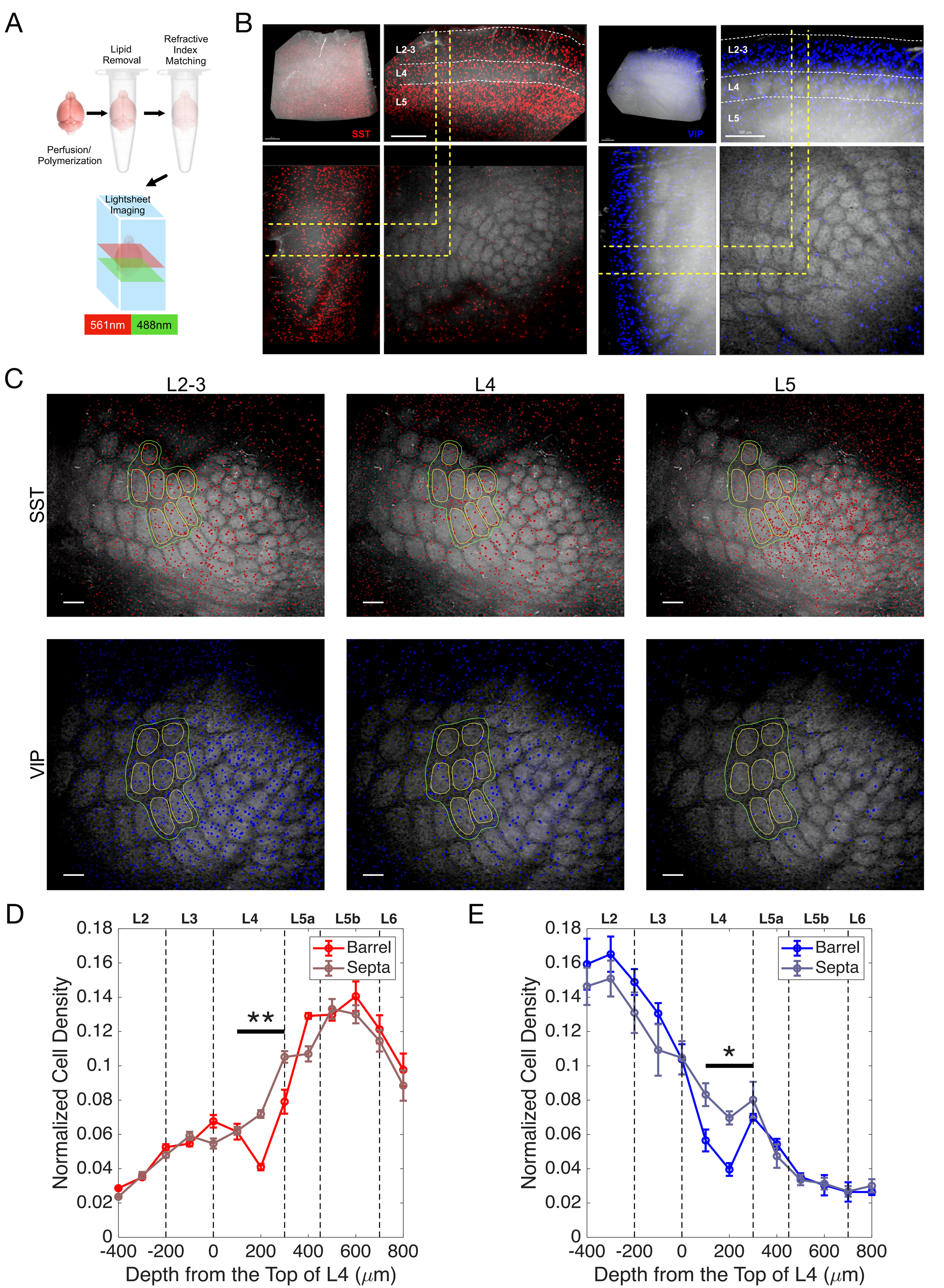
A
Lipid Removal
Refractive Index Matching
Perfusion/ Polymerization
Lightsheet Imaging
561nm
488nm
B
SST
L2-3
L4
L5
VIP
C
L2-3
L4
L5
SST
VIP
D
L2
L3
L4
L5a
L5b
L6
Barrel
Septa
**
Normalized Cell Density
Depth from the Top of L4 (μm)
E
L2
L3
L4
L5a
L5b
L6
Barrel
Septa
*
Normalized Cell Density
Depth from the Top of L4 (μm)

Figure 2

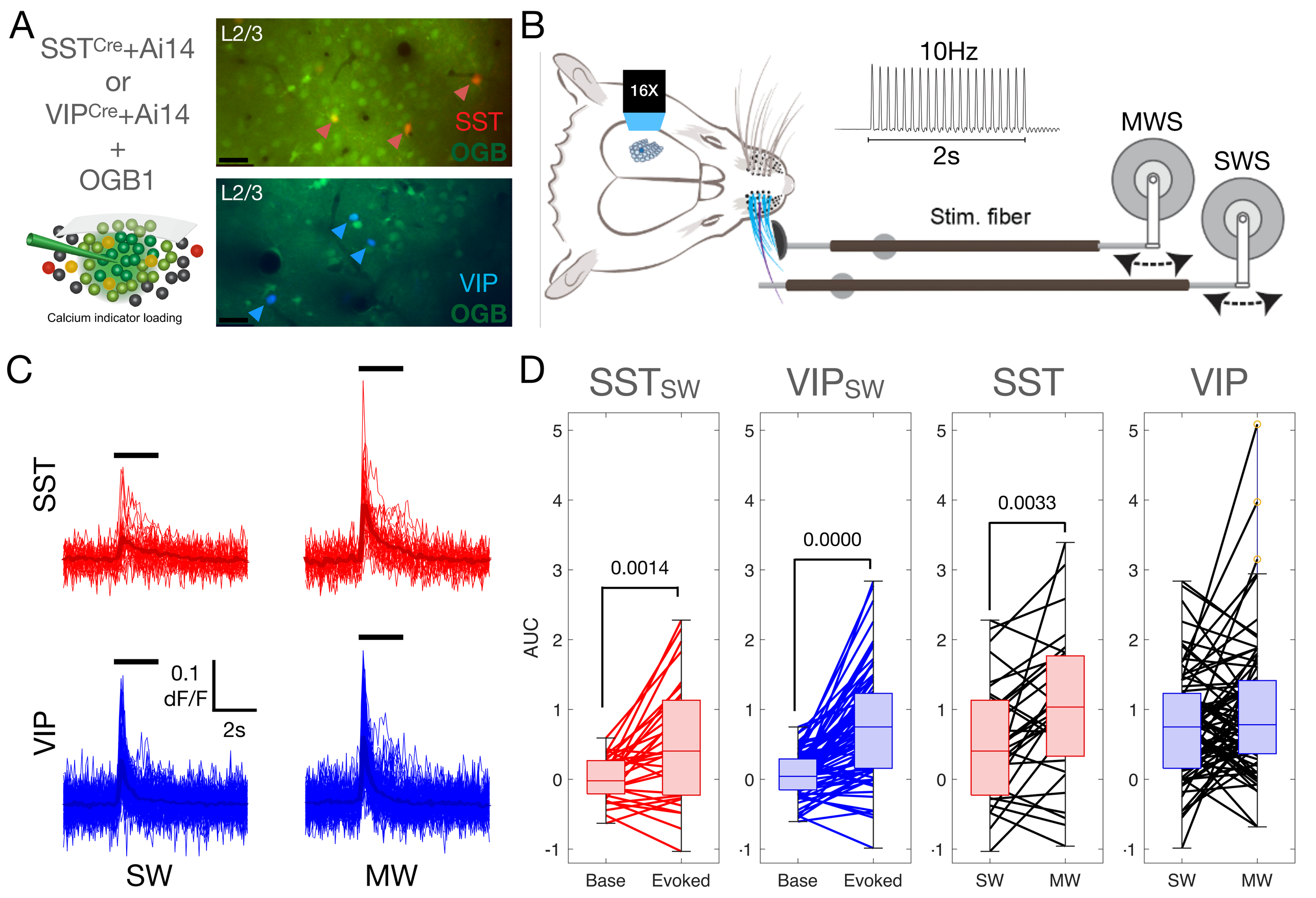
A
SST^{Cre}+Ai14
or
VIP^{Cre}+Ai14
+
OGB1
Calcium indicator loading
L2/3
SST
OGB
L2/3
VIP
OGB
B
16X
10Hz
2s
MWS
SWS
Stim. fiber
C
SST
VIP
0.1
dF/F
2s
SW
MW
D
SST$_{SW}$
VIP$_{SW}$
SST
VIP
AUC
0.0014
0.0000
0.0033
Base
Evoked
Base
Evoked
SW
MW
SW
MW

Figure 3

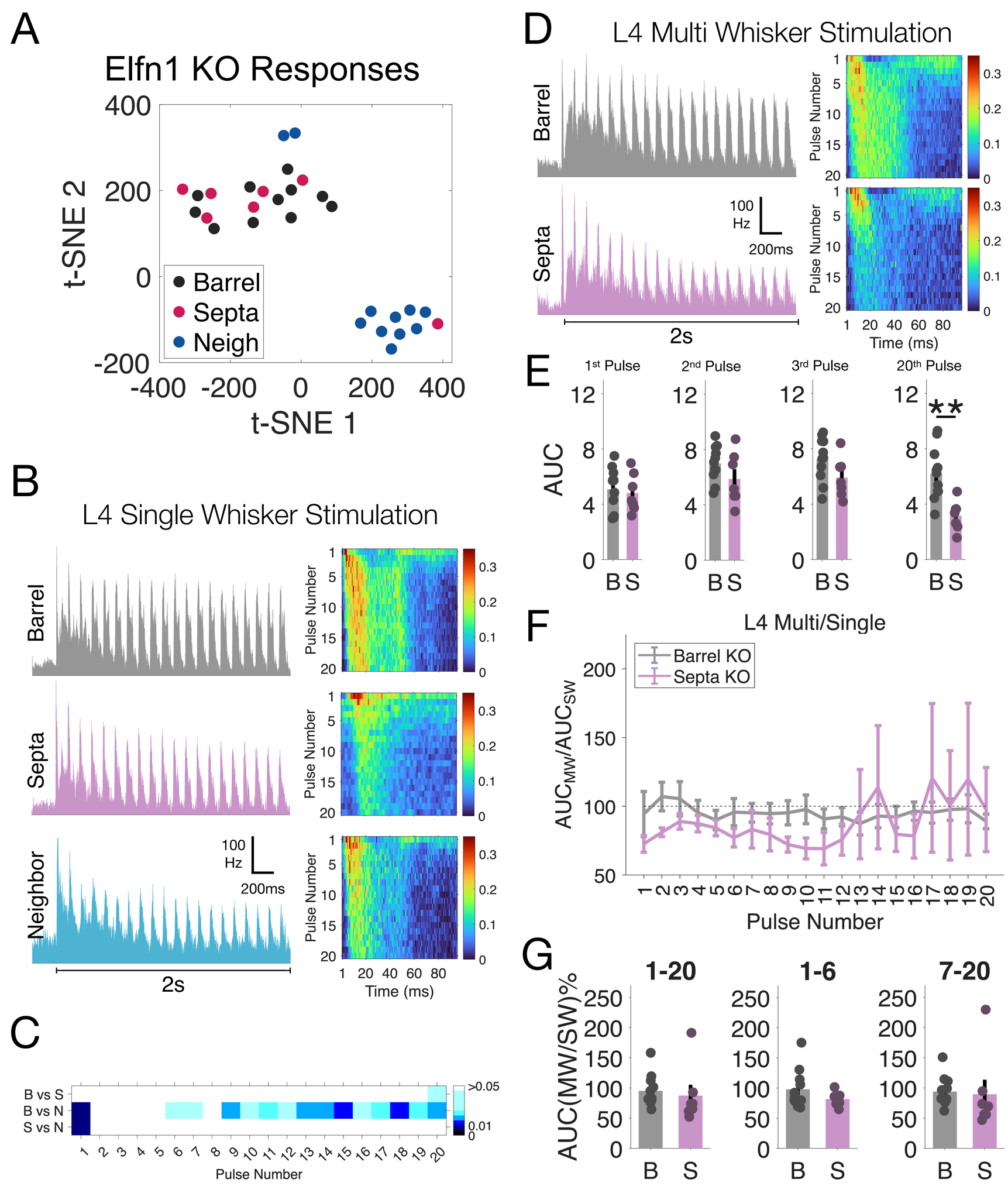
A
Elfn1 KO Responses
t-SNE 2
t-SNE 1
Barrel
Septa
Neigh
B
L4 Single Whisker Stimulation
Barrel
Septa
Neighbor
100 Hz
200ms
2s
Pulse Number
Time (ms)
C
B vs S
B vs N
S vs N
Pulse Number
D
L4 Multi Whisker Stimulation
Barrel
Septa
100 Hz
200ms
2s
Pulse Number
Time (ms)
E
1st Pulse
2nd Pulse
3rd Pulse
20th Pulse
AUC
B S
F
L4 Multi/Single
Barrel KO
Septa KO
AUC_MW/AUC_SW
Pulse Number
G
1-20
1-6
7-20
AUC(MW/SW)%
B S

Figure 4

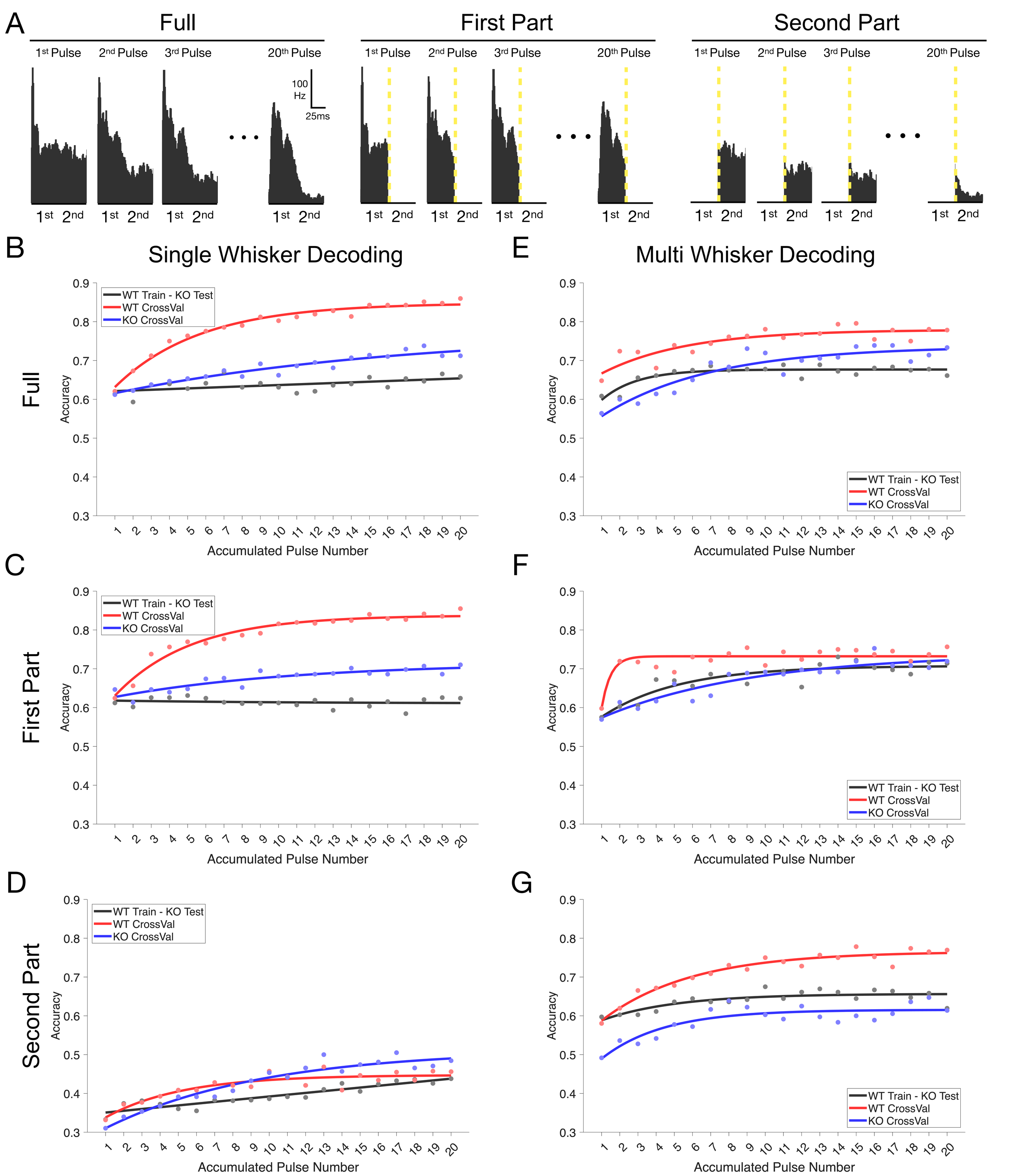
A
Full
First Part
Second Part
1st Pulse
2nd Pulse
3rd Pulse
20th Pulse
100 Hz
25ms
1st 2nd
B
Single Whisker Decoding
E
Multi Whisker Decoding
Full
C
First Part
D
Second Part
G
WT Train - KO Test
WT CrossVal
KO CrossVal
Accuracy
Accumulated Pulse Number

Figure 5

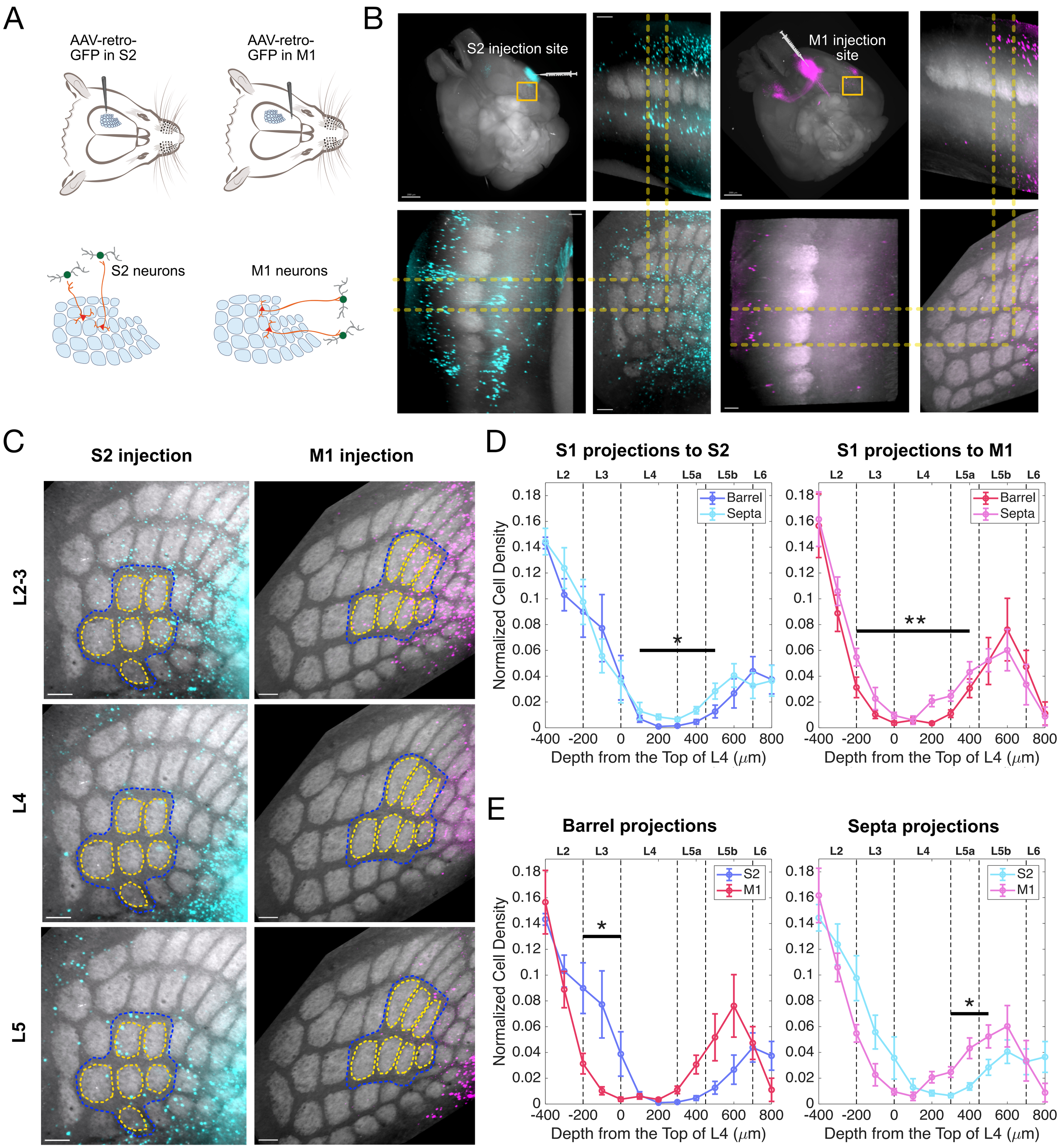
A
AAV-retro-GFP in S2
AAV-retro-GFP in M1
S2 neurons
M1 neurons
B
S2 injection site
M1 injection site
C
S2 injection
M1 injection
L2-3
L4
L5
D
S1 projections to S2
S1 projections to M1
L2
L3
L4
L5a
L5b
L6
Barrel
Septa
Normalized Cell Density
Depth from the Top of L4 (μm)
*
**
E
Barrel projections
Septa projections
S2
M1

Figure 6

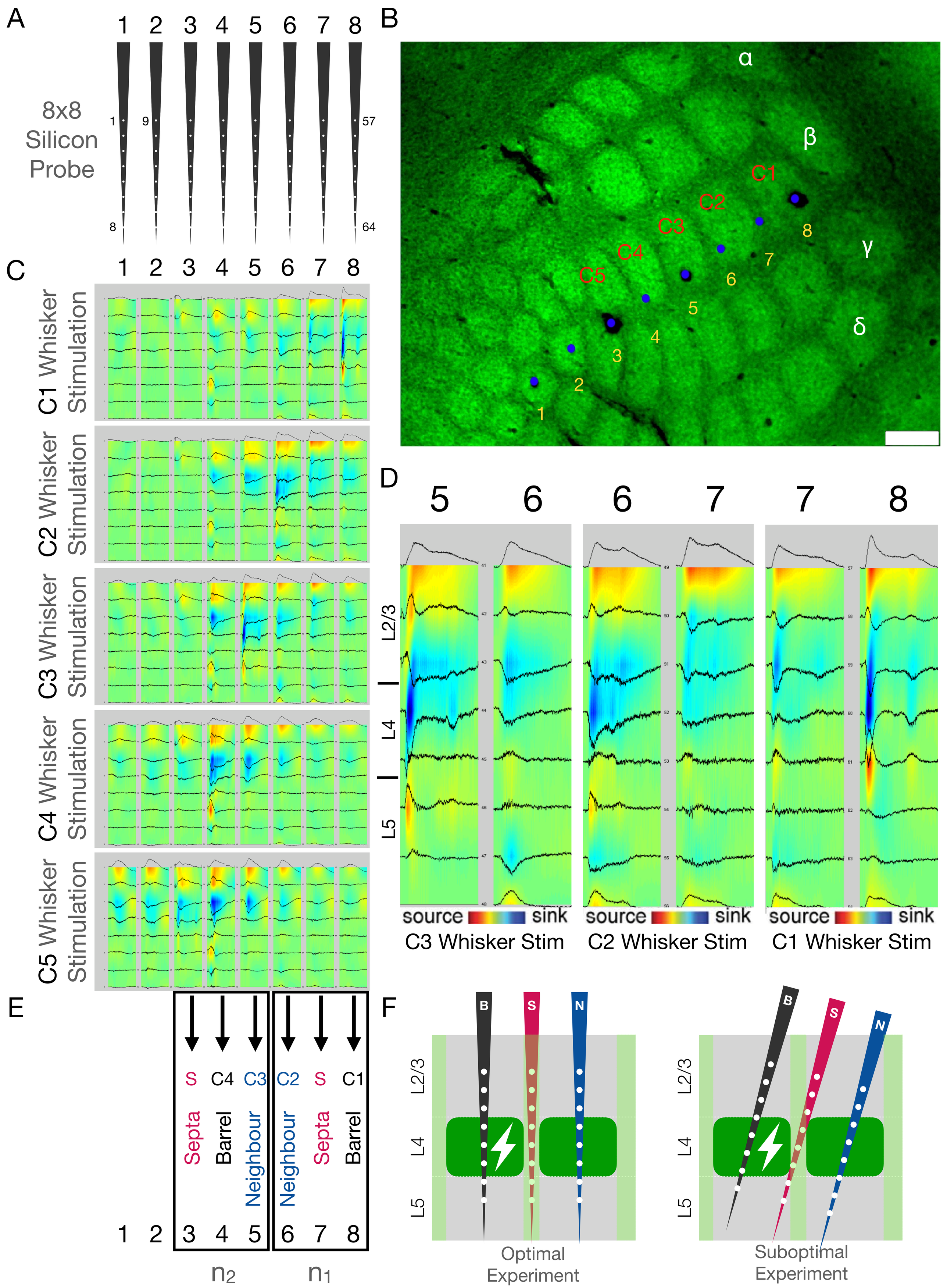

Supplementary Figure 1

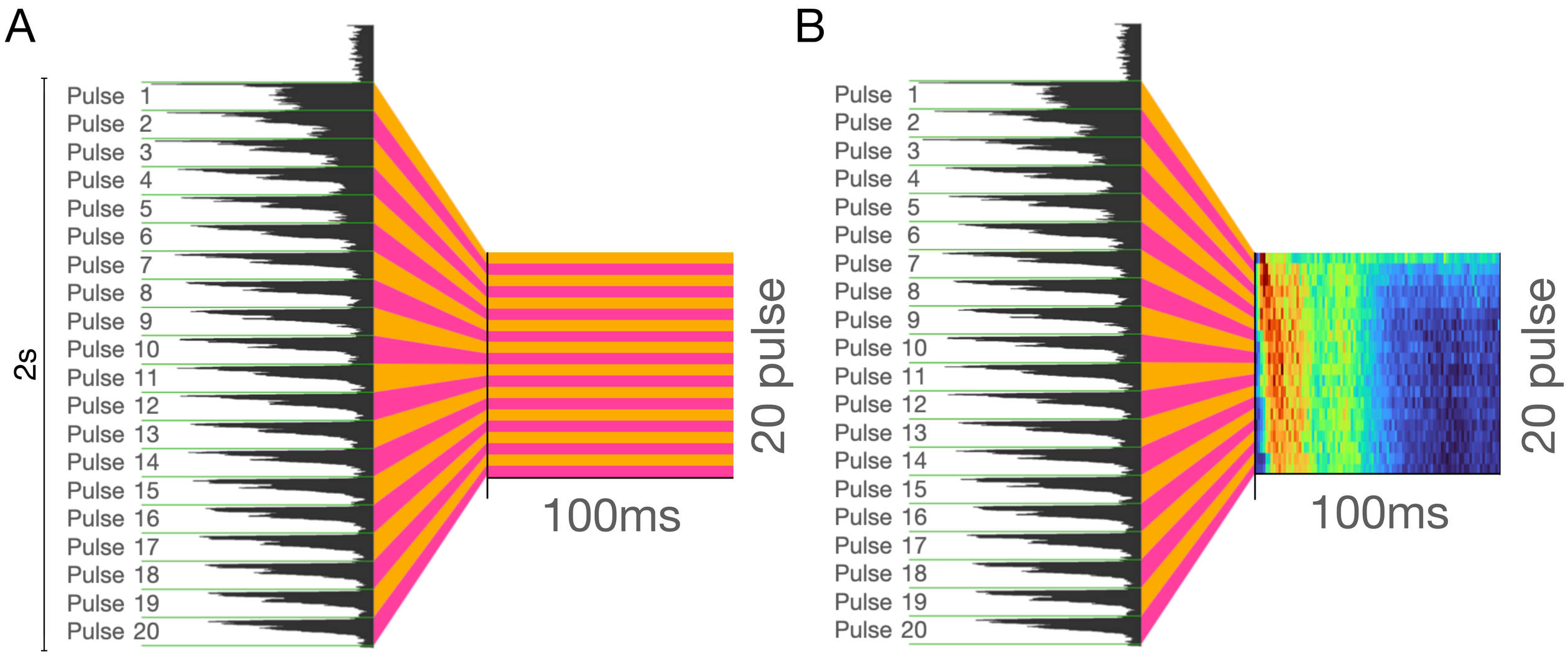

Supplementary Figure 2

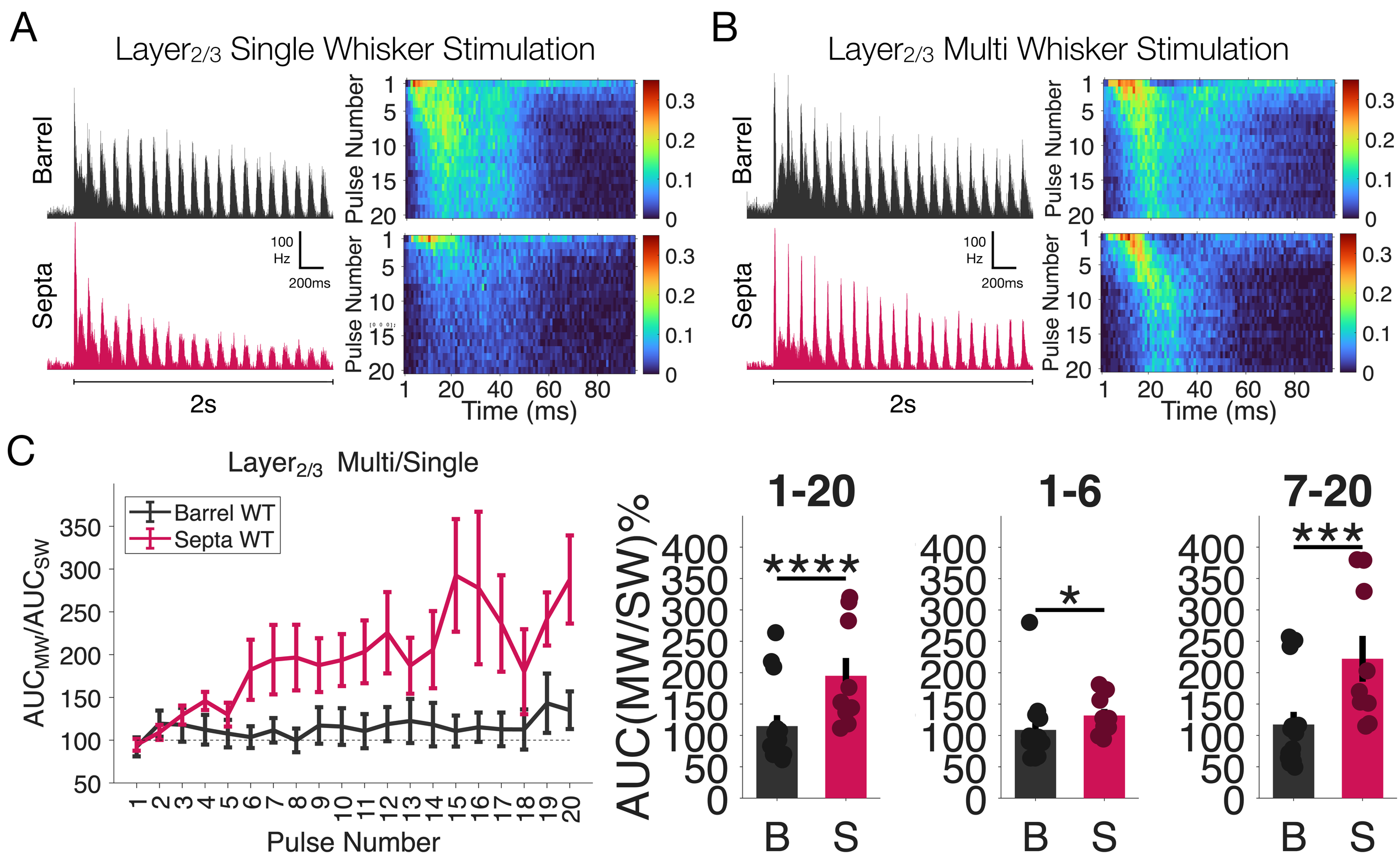

Supplementary Figure 3

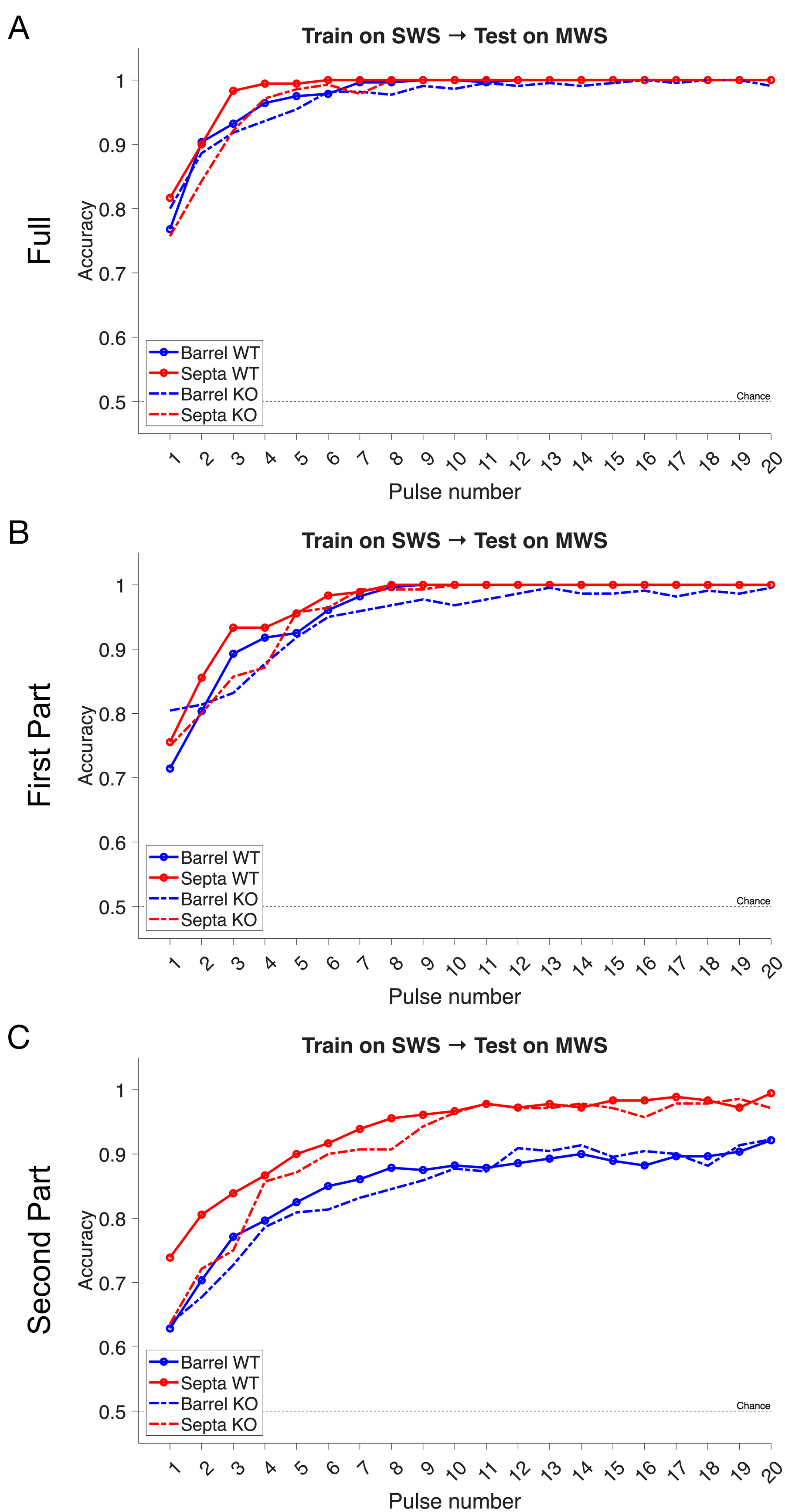

Supplementary Figure 4